MOTION AND EVOLUTION OF THE CHAOCHOU FAULT, SOUTHERN TAIWAN

A Thesis

by

LAUREN E. HASSLER

Submitted to the Office of Graduate Studies of
Texas A&M University
in partial fulfillment of the requirements for the degree of

MASTER OF SCIENCE

August 2004

Major Subject: Geology

MOTION AND EVOLUTION OF THE CHAOCHOU FAULT,

SOUTHERN TAIWAN

A Thesis

by

LAUREN E. HASSLER

Submitted to Texas A&M University
in partial fulfillment of the requirements
for the degree of

MASTER OF SCIENCE

Approved as to style and content by:

David V. Wiltschko (Chair of Committee)	Julie Newman (Member)
Vatche P. Tchakerian (Member)	Richard L. Carlson (Head of Department)

August 2004

Major Subject: Geology

ABSTRACT

Motion and Evolution of the Chaochou Fault, Southern Taiwan. (August 2004)
Lauren E. Hassler, B.S., Appalachian State University
Chair of Advisory Committee: Dr. David V. Wiltschko

The Chaochou Fault (CCF) is both an important lithologic boundary and a significant topographic feature in the Taiwan orogenic belt. It is the geologic boundary between the Slate Belt to the east, and the Western Foothills to the west. Although the fault is known to be a high angle oblique sinistral thrust fault in places, both its kinematic history and its current role in the development of the orogen are poorly understood. Field fabric data suggest that structural orientations vary along strike, particularly in the middle segment, the suspected location of the intersection of the on-land Eurasian continent-ocean boundary and the Luzon Island Arc. Foliation/solution cleavage is oriented NE-SW and in the northern and southern sections, but ESE-WNW in the middle segment. Slip lineations also reveal a change in fault motion from dip-parallel in the north to a more scattered pattern in the south. This correlates somewhat with recent GPS results, which indicate that the direction of current horizontal surface motion changes along strike from nearly perpendicular to the fault in the northern field area, to oblique and nearly parallel to the fault in the southern field area. The magnitude of vertical surface motion vectors, relative to Lanyu Island, decreases to the south. Surface morphology parameters, including mountain front sinuosity and valley floor width/valley height ratio indicate higher activity and uplift in the north. These observations correlate well with published apatite/zircon fission track data that indicate un-reset ages in the south, and reset ages in the northern segment. Geodetic and geomorphic data indicate that the northern segment of the CCF and Slate Belt are currently undergoing rapid uplift related to oblique arc-continent collision between the Eurasian continent and the Luzon arc. The southern segment is significantly less active perhaps because the orogen is not yet involved in direct arc-continent collision.

ACKNOWLEDGEMENTS

Thanks to my thesis advisor, Dr. David Wiltschko , and to my committee, Dr. Julie Newman and Dr. Vatche Tchakerian, for their guidance and assistance on this project. Thanks to Dr. Jih-Hao Hung and his students in Taiwan for their assistance in the field. Thanks to John Spang for assistance with the cross sections. Thanks to Lai Lee for help with ArcGIS and for her friendship. Thanks also to Dr. Will Lamb for use of the petrographic microscope. Many sincere thanks to my colleagues in Tectonophysics. My research has greatly benefited from discussions with you all. Thanks to Dr. Richard Allmendinger for use of his Stereonet software. This project was supported by the NSF Summer Institute in Taiwan and grants from AAPG and GSA.

TABLE OF CONTENTS

LIST OF FIGURES

1. INTRODUCTION

The transition from accretion to collision of an accretionary prism, forearc, and arc at a subduction zone is a fundamental feature of arc-continent collisions. Structures from each of these transitional stages of collision are often, but not necessarily obscured by later events. Reconstructing these stages and their evolution can pose a challenge (e.g., Rowley and Kidd, 1981; Anczkiewicz et al., 2000; Brown et al., 2001; among many others). In the case of Taiwan, the Luzon volcanic arc system is colliding with the East Eurasian margin (Fig. 1). Collision in Taiwan is oblique and therefore is closing from north to south in zipper-like fashion (Suppe, 1984). Because the orogen is developing to the south, there is a space-time equivalence where structures may be traced from the onset of collision (south) to maturity (north) as the nature of the orogen changes progressively from submarine intra-ocean subduction south of 21 20' N, to arc-continent collision between about 21 20'N and 23 N, and to arc accretion north of about 23 N.

The Chaochou Fault (CCF) is one structure that persists through the transition from accretion to collision and appears to be a fundamental boundary from the inception of the Taiwan orogen. It can be traced based on bathymetry from off the southern coast of Taiwan, where the collision is just beginning, to the northernmost tip of the island (Liu et al., 1997; Fuh et al., 1997). On land the CCF is a major province boundary between the sedimentary fold and thrust belt to the west, the Western Foothills, and the metamorphosed Slate Belt of the Central Range to the east (Fig. 2). The transition from accretion to collision may occur near 23°N latitude, where a transition is marked by changes on the upthrown side of the Chaochou Fault in a) structural orientations such as fold axes and rock fabrics, b) slip orientations and rates on faults, c) surface morphology, d) seismicity.

This thesis follows the style of the journal Tectonophysics.

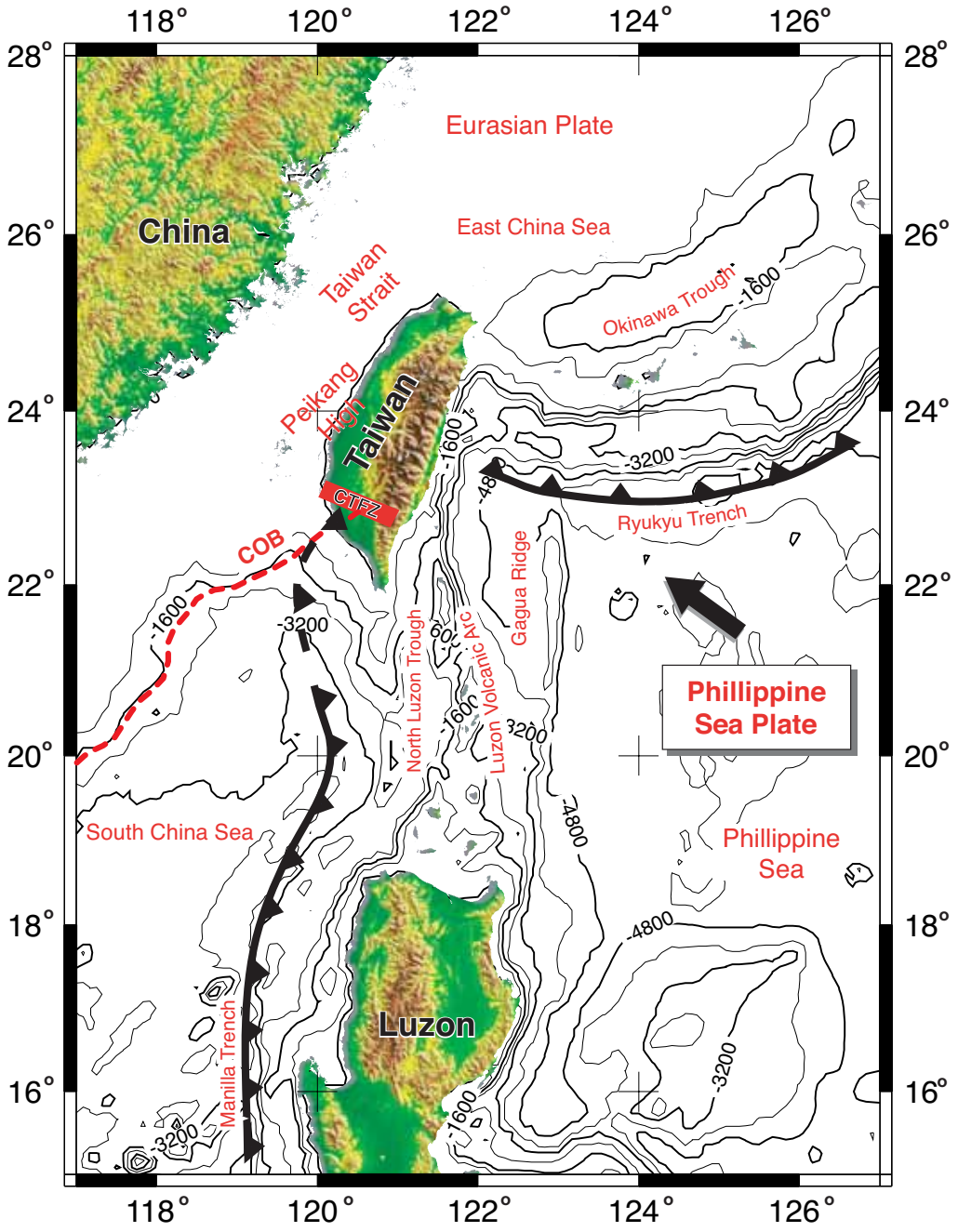

Fig. 1. Map showing geographic and plate tectonic setting of Taiwan. Note the opposing subduction systems, the Ryukyu Trend in the north and the Manila Trench in the west. The onland trace of the Manila Trench is not shown and is not precisely known. The continent-ocean boundary (COB) is shown (after Lallemand et al., 2001). The continental margin is oriented N60E, whereas the Luzon arc strikes N10E and moves in a N50W direction. The angle between the plate convergence vector and the margin is on average 70 degrees.

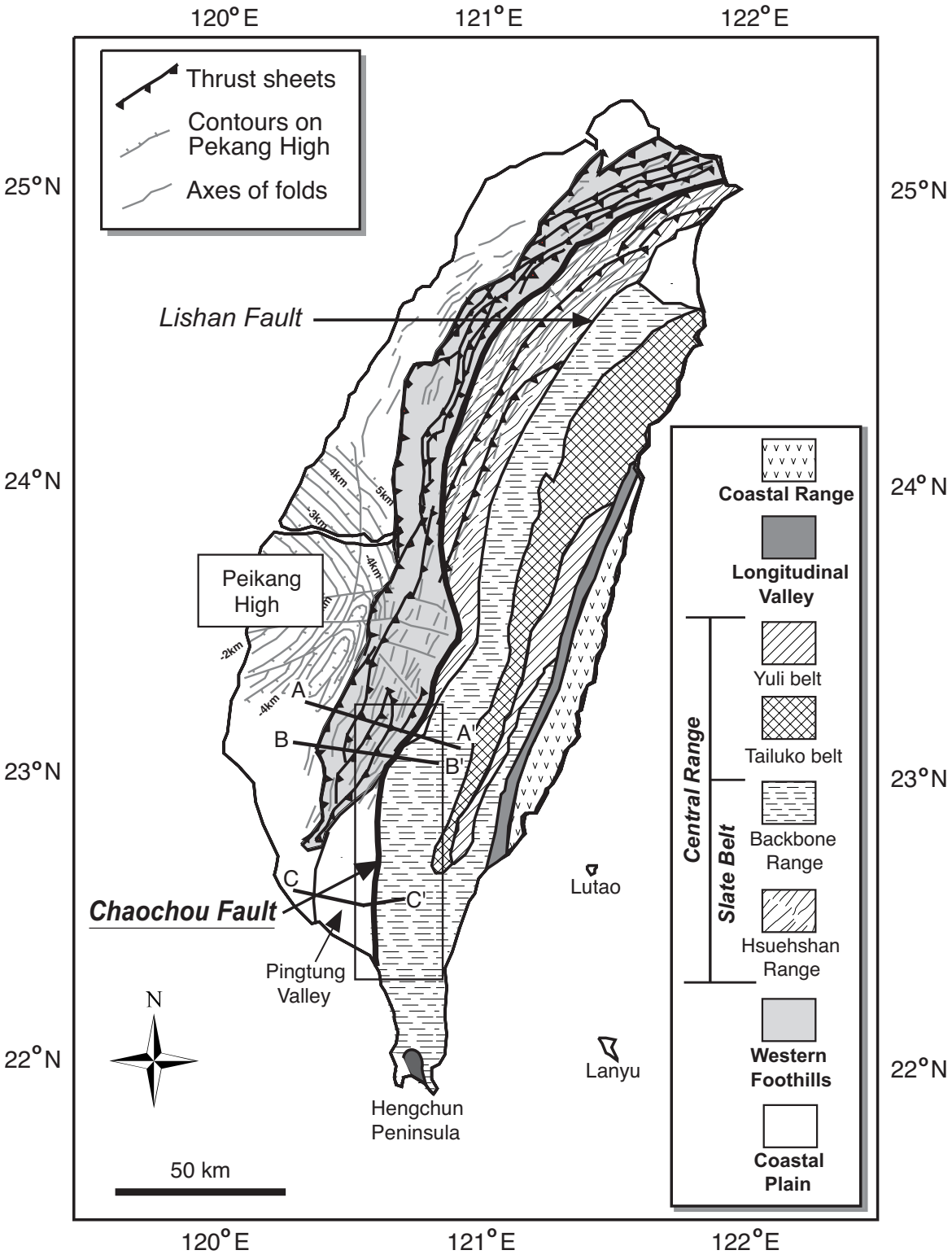

Fig. 2. Index map showing the geology of Taiwan and the study area. Note the location of the Chaochou Fault; particularly the bend at approximately N 23□ latitude. Note also the location of the Peikang basement high in west central Taiwan. Map modified from Sibuet and Hsu, 1997.

The goal of this study is to describe past, recent, and present deformation associated with the CCF in Southern Taiwan by integrating structural and petrographic data and landscape morphology with available GPS, seismicity, and fission track data. This study will focus on this southern extent of the CCF (Fig. 2). Of particular interest is the region near the town of Liukuei, where the fault takes a sharp bend toward the south. In addition to a change in surface expression of the fault, this restraining bend is associated with changes in rock fabric orientations, surface morphology, surface velocity, and seismicity.

1.1 Tectonic Setting of Taiwan

The island of Taiwan is the result of southward propagating oblique collision between the Luzon Island Arc, on the Philippine Sea Plate (PSP), and the eastern margin of Eurasia (Fig. 1, Teng, 1990). The PSP is currently advancing toward Eurasia from the southeast, between 7 and 9 cm per year, relative to the East Asian margin (Seno et al., 1987, Yu et al., 1997, Hickman et al, 2002, Wiltschko et al., 2002, Rau and Wu, 1995, Teng, 1990).

The north-facing Ryukyu subduction zone and associated backarc spreading dominate tectonic processes in the north. In the south, the Eurasian plate is subducting eastward, beneath the PSP (Teng, 1990). The change in subduction polarity occurs below the Hualien region of northeastern Taiwan (Fig.1). A well-defined Benioff zone beneath Northern Taiwan corresponds to the down-going PSP slab of the Ryukyu subduction system (Rau and Wu, 1995). Somewhat less clearly defined is the Benioff zone along the length of the island that corresponds to the down-going Eurasian slab.

Teng et al. (2000) have proposed a southward-propagating tear in the down-going Eurasian slab as a mechanism for the “flip” in subduction polarity beneath Taiwan. As the breakaway slab continues sinking into the mantle, the north-facing Ryukyu slab propagates westward into the opening. The timing of the onset of slab

breakoff, the rate of its propagation, and the current extent of are still unclear (Rau and Wu, 1995, Teng et al., 2000, Lallemand et al., 2001).

A tomographic section through the field area for this study clearly shows a dense slab of Eurasian crust subducting eastward beneath the island (Fig. 3, Lallemand et al., 2001). The downgoing slab is not everywhere continuous with depth. In the image shown, a zone of low density at the top of the slab indicates that it may not be attached, and that a tear may well have propagated as far south as our study area (Rau and Wu, 1995). Also note that while tomography from Northern Taiwan indicates a mature crustal root beneath the Central Range (Fig. 2), a dense mountain root is absent in the south (Rau and Wu, 1995). The southern portion of the island may not yet be involved in direct arc-continent collision.

Precollisional extension of the South China continental margin is well documented (Teng, 1990; Tillman et al., 1992; Lu, 1992; among others). Sibuet and Hsu, (1997), identify four different belts of basins in the South China Sea that formed during the Early Miocene and subsequently changed opening direction from N-S to NW-SE (Pautot et al., 1986 in Sibuet and Hsu, 1997). Also at this time, Luzon Island was forming as part of the Luzon Island Arc (Sibuet and Hsu, 1997).

Collision began in the region that is now northern Taiwan around 20 Ma, and peaked between 8 and 5 Ma (Teng, 1990). This peak in collision intensity corresponds to a change in the direction of motion of the Philippine Sea Plate from NNW to WNW and resulted in a more direct, orthogonal collision (Teng, 1990). At this time, the stratigraphy of the Coastal Range (Fig. 2) shows a change from volcanic arc sediments to continental-derived sediments in the lower Pliocene (Chen and Wang, 1988 in Teng, 1990). In addition, in the Western Foothills (Fig. 2), eastward prograding sediments derived from Eurasia become westward prograding foreland basin sediments as the Central Range was rapidly uplifted above sea level (Chi and Huang, 1981 in Teng, 1990). Sediment supply increased drastically in both regions during the Pliocene (Teng, 1990).

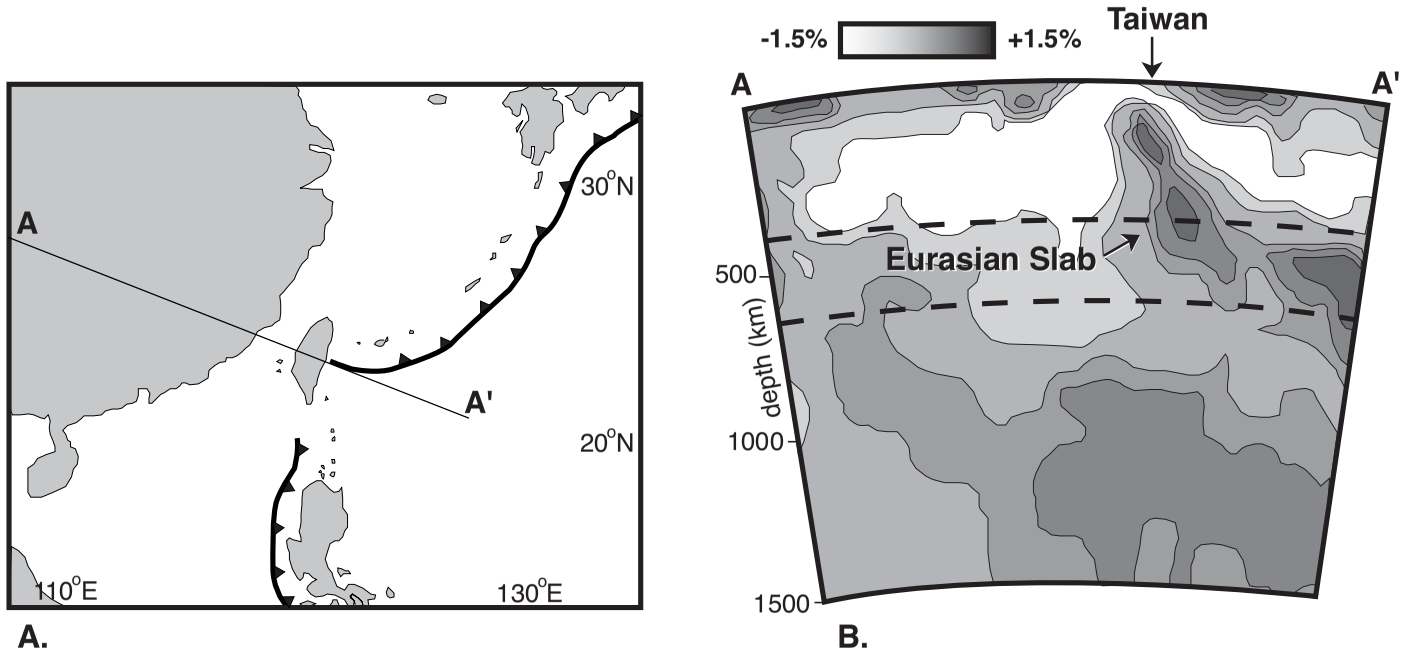

Fig. 3. Seismic tomographic section across the study area in southern Taiwan. A low velocity anomaly appears between the surface and the down-going South China Sea slab indicating that the slab is not attached. Modified from Lallemand, 2001.

There is no syncollisional sedimentary record for the Central Range as this area was presumably exposed during the earliest stages of collision and hence was eroding. Radioisotope and zircon/apatite fission track dating indicate deep burial before collision, followed by rapid uplift around 3 Ma, during peak collision (Lin, 1982, in Teng, 1990, and Liu et al., 2001). The basement rocks of the Tananao Complex underwent Greenschist facies metamorphism during peak collision and have since been exhumed from approximately 13 km (Ernst, 1983, Wang et al., 1982, in Teng, 1990).

Seismicity varies throughout the island. Most focal mechanisms from southern Taiwan are consistent with a NW-SE compressive stress from PSP collision (Yeh et al., 1991, Rau and Wu, 1998). Focal mechanisms in the Longitudinal Valley indicate sinistral slip motion, which corresponds with plate motion (Yeh et al., 1991). At least one right lateral mechanism is found in southern Taiwan, in the Pingtung Valley region, perhaps indicating extrusion to the south (Kao and Jian, 2001). Strike-slip faulting occurs in southern Taiwan beneath the Central and Foothills Ranges (Kao and Jian, 1991), south of what has been called the Chuchi Transfer Fault Zone (Lacombe et al., 2001). This boundary represents a major change in the character of seismicity in Taiwan. Although the nature of this boundary is not known, it may represent the southern extent of direct arc-continent collision in Taiwan.

1.2 Southern Taiwan Geology

The Taiwan orogenic belt is divided into four geologic provinces (Fig. 2; Ho, 1986). From east to west they are the Coastal Range, the Central Range (subdivided into the Tanzania Complex and Slate Belt), the Western Foothills Range, and the Coastal Plain. The Coastal Range is made up of accreted Luzon Volcanic Arc material overlain by syncollisional sediments of Late Miocene to Pleistocene age (Teng, 1990). The Coastal Range is bounded on west by the Longitudinal Valley Fault (LVF) system, which is thought to be the surface expression of the Eurasian/PSP boundary (Teng, 1990). The Central Range, bounded on the east by the Longitudinal Valley Fault, and on

the west by the Chaochou Fault, is divided into two provinces, the Tananao Complex and the Slate Belt. The Tananao Complex represents the metamorphosed eastern Eurasian continental basement (Teng, 1990). The metamorphic grade in the Tananao Complex increases from Prehnite-Pumpellyite facies in the west to Greenschist and Blueschist facies in the east. The Slate Belt, subdivided into the Backbone and Hsuehshan ranges, represents the tectonized Cenozoic sedimentary east Asian basement cover, and is composed of Paleocene to Miocene slates, argillites, and quartzites (Ho, 1986). The Backbone Range to the east consists of Eocene to Miocene pelitic sediments, which are thought to be more distal to the continental margin than those of the Hsuehshan Range (Tillman et al., 1992, Lee et al., 1997). The Hsuehshan Range grades from Prehnite-Pumpellyite facies in the west to Greenschist facies in the east. The Hsuehshan Range, which is composed of predominantly Eocene and Oligocene continental margin sediments and bound to the east by the Lishan Fault, may be a large, left-laterally sheared pop-up structure, possibly and inverted Neogene basin formed during a period of extension in the South China Sea (Biq, 1989; Clark et al., 1992; Tillman and Byrne, 1995). The range is a structural as well as geographic high, being bound to the east and west by younger units in the Western Foothills and Slate Belt respectively (Clarke et al., 1992). Going east across the Lishan Fault, to the Backbone Range, the metamorphic grade changes back to Prehnite-Pumpellyite facies (Lee et al., 1997). The Western Foothills consist of folded and thrust faulted precollisional continental shelf sediments and westward prograding, syncollisional clastics that collected in a rapidly subsiding foreland basin (Teng, 1990). Sedimentary units decrease in thickness from greater than 8000 m in the east to 500 m in the west. Units typically coarsen and thicken to the south where uplift began later than in the north (Ho, 1986). The Western Foothills are separated from the Slate Belt by the Chaochou Fault, the focus of this study.

1.3 The Chaochou Fault

The Chaochou Fault is a major mid-orogen fault between the Western Foothills and Central Range. The main trace of the fault is known by several names, e.g. Chuchi, Suantung, Tulungwan, and Hungchun among them. In the south it is known as the Chaochou Fault (Yen and Tien, 1986). In the south, the fault separates the Slate Belt from the Pingtung Valley, which has been interpreted as a down-dropped Neogene basin, filled with alluvial and fluvial material shed from the Western Foothills and Central Ranges to the north (Fig. 2, Ho, 1986). Initial gravity surveys in southern Taiwan identified the CCF as a high-angle reverse fault, dipping to the east at around 75 to 80 degrees (Chiang, 1971). Biq (1989) interprets the fault as an oblique wrench fault with components of both sinistral and reverse-slip motion. This assessment is based on the occurrence of left-lateral splay faults that branch off from the main CCF in the north and the occurrence of peaks of relatively high elevation on the eastern side of the fault with associated gravity anomalies that indicate crustal thickening. Recent GPS data indicate that the obliquity of motion changes along trace of the fault (Wiltschko et al., 2002). Both vertical and horizontal motion associated with the fault changes along its strike and low convergence on either side of the fault indicates that it is high angle (Wiltschko et al., 2002).

1.4 Cross Sections

In order to illustrate the upper crustal structure across the CCF, we present three cross sections from southwestern Taiwan. These sections cross the study area in the northern, middle, and southern regions and were chosen to illustrate the development of the orogen from south to north (Fig. 2). Geologic maps of the region provide surface geology from which we infer sub-surface structure (see figure captions for details). Each section extends to a depth of approximately 12 to 15 km and ranges 40 to 85 km in length and assumes displacement from the ESE. These cross sections complement those

of Hickman et al. (2002), but our interpretation yields less shortening. We extend the lines into the Slate Belt both to illustrate our interpretation of the CCF geometry at depth.

Stratigraphy is summarized in Figure 4. For a modified geologic map and section locations, see Figure 5. Variations in stratigraphic thickness of units represented in these sections may occur where extensional basement faults have created additional accommodation space prior to collision. However, well data are too sparse to document these changes. Therefore, units are drawn with uniform thicknesses throughout the three cross sections. We have placed a basal detachment at approximately 13 km below sea level to the southeast rising to 10 km in the northwest in all three lines. No seismic or well data confirms the location of this detachment. However, this is a minimum depth to accommodate stratigraphy and structures exposed at the surface.

1.4.1 Line A-A'

Line of section A-A' (Fig. 6) crosses the northern extension of the Nuishan anticline, which is cut by the Lunhou fault and a small splay. The Lunhou fault places the Miocene Tangenshan sandstone on top of the Pliocene Peliao shale and accommodates approximately 3 km of displacement. Because the surface trace indicates it is low angle, the Kouhsiaoli fault is interpreted as a backthrust to the Lunhou fault. We add another small, blind splay fault in the footwall of the Lunhou fault to account for west-dipping beds observed at the surface. We draw this splay flattening at the base of the Chutouchi formation and ramping up again to form a small fault propagation anticline at the westernmost extent of the Western Foothills.

Stratigraphic offset indicates displacement on the Chutouchi fault is approximately 2 km. The Chutouchi fault is shown to cut up-section from the basal detachment and utilizes east-dipping bedding in the hanging wall anticline east of the Lunhou fault. This interpretation implies out of sequence faulting of the Chutouchi fault.

To accommodate stratigraphy seen at the surface, we interpret a large section of basement carried by the Pingchi fault. As drawn, the Pingchi fault accommodates 5 km

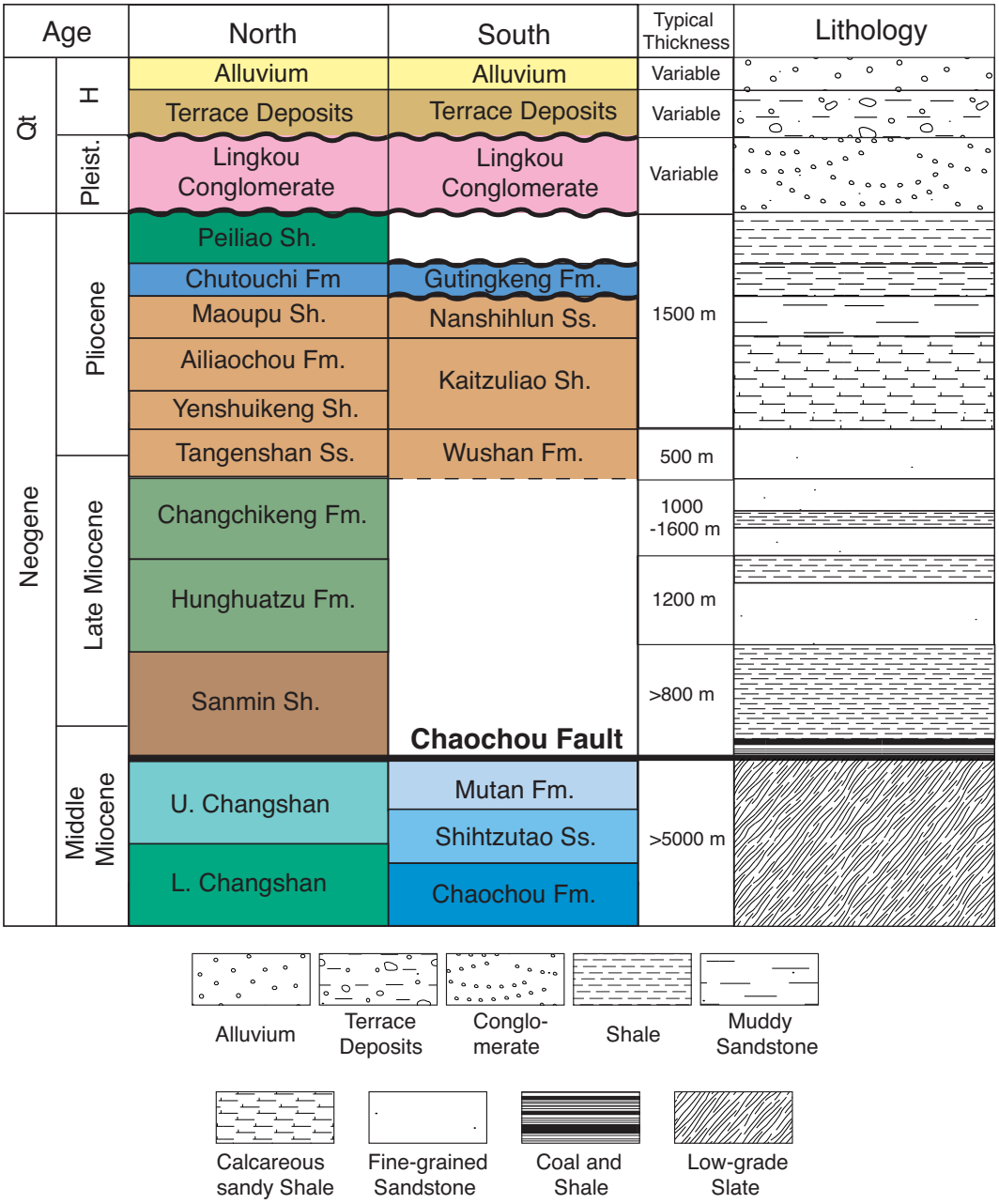

Fig. 4. Field area stratigraphy. Modified from Ho, 1986, and CPC Map 6, Tainan, 1989. Stratigraphy is compiled from CPC geologic maps of southwest Taiwan, Kaohshiung-Pingtung and Tainan Sheets (1992, 1989), CGS geologic maps 51 (Chiasien) and 67 (Fangliao) (2000, 1993), and Ho, 1986. Detailed lithologic descriptions are published in Ho, 1986.

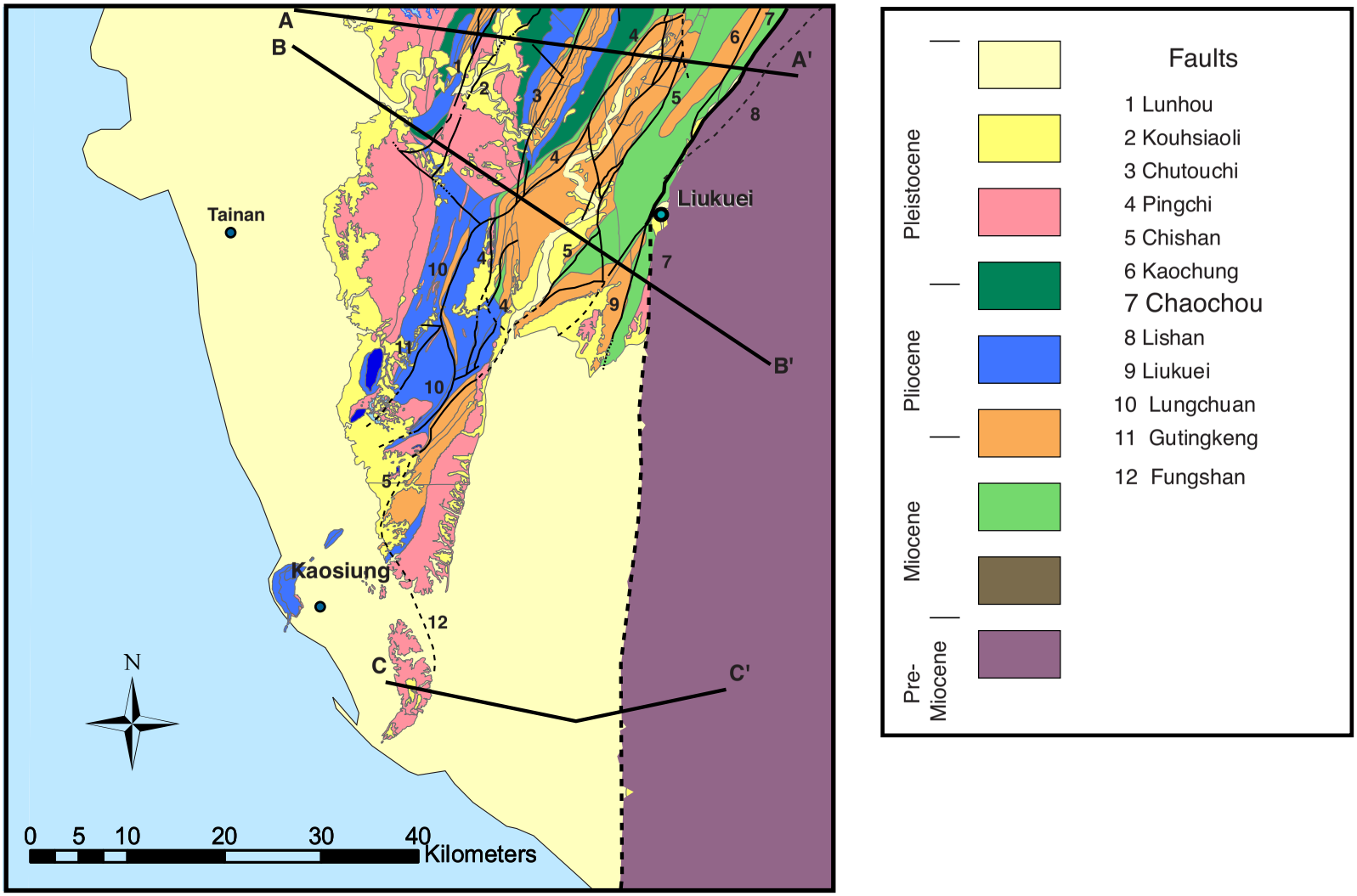

Fig. 5. Geologic map and locations of cross sections. Modified from Ho, 1986, and CPC Map 6, Tainan, 1989. Stratigraphy is compiled from CPC geologic maps of southwest Taiwan, Kaohshiung-Pingtung and Tainan Sheets (1992, 1989), CGS geologic maps 51 (Chiasien) and 67 (Fangliao) (2000, 1993), and Ho, 1986. Detailed lithologic descriptions are published

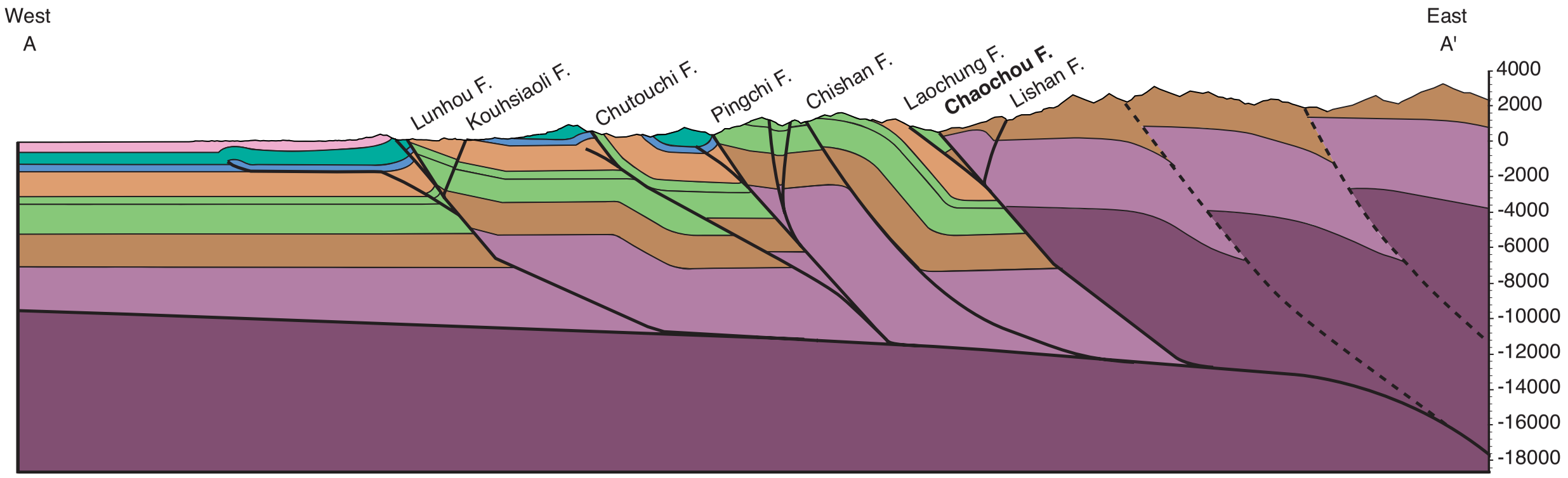

Fig. 6. Line of Section A-A'. Cross sections across the Western Foothills and Slate Belt in Southern Taiwan. Structural and stratagraphic data from CPC geologic maps 6 (Tainan) and 7 (Kaohshiung-Pingtung), and CGS geologic maps 67 (Fanglio) and 51 (Chiahsien), stratigraphic descriptions in Ho, 1989, nearby wells, and one seismic section across the eastern Pingtung Valley by Chang, 1971. No vertical exaggeration.

of displacement. We draw a small blind thrust fault from the Pingchi fault into the footwall to produce the west-dipping beds observed at the surface. Several small faults with minor amounts of displacement cut the Pingchi hanging wall block. These faults are interpreted as splay faults to the Pingchi. The Chishan fault may utilize bedding in the Pingchi hanging wall anticline. This interpretation is developed further in the cross section for line B-B'.

The Kaochung fault is shown here as a small splay to the CCF and is perhaps a precursor to the CCF. The CCF is interpreted here as a steeply-dipping reverse fault that cuts up-section from the basal detachment after ramping up from a deeper portion of the basement. This geometry allows for approximately 10 km of shortening in the Western Foothills and exhumes pre-Miocene basement, which is exposed in the Eastern Central Range. The Lishan fault merges with the CCF south of line B-B' and is shown here as a backthrust to the CCF. The region between the CCF and the Lishan fault is the southern extension of the Hsuehshan Range.

Slate Belt rocks adjacent to the CCF are early- to mid-Miocene in age (CGS maps 67 and 51) and are brought up from at least 13 km in order to produce the reset Zircon fission track ages observed by Liu, 2001 and Fuller, 2003. The Slate Belt is not mapped in detail in the region through which line A-A' passes. Therefore, units are not differentiated in the cross section.

1.4.2 Line B-B'

Line B-B' (Fig. 7) crosses the Lunhou and Kouhsiaoli faults 12 km south of line A-A'. In the B-B' cross section, both faults are interpreted to dip westward. The Kouhsiaoli fault, no longer a backthrust as in line A-A', forms a steep reverse fault. The Lunhou fault places Pleistocene units above Pliocene with approximately 2 km of displacement, less than in the northern, A-A' section. The small, blind splay fault is still present in the footwall, but we interpret it to have stepped up-section to the Late Pliocene Chutouchi formation.

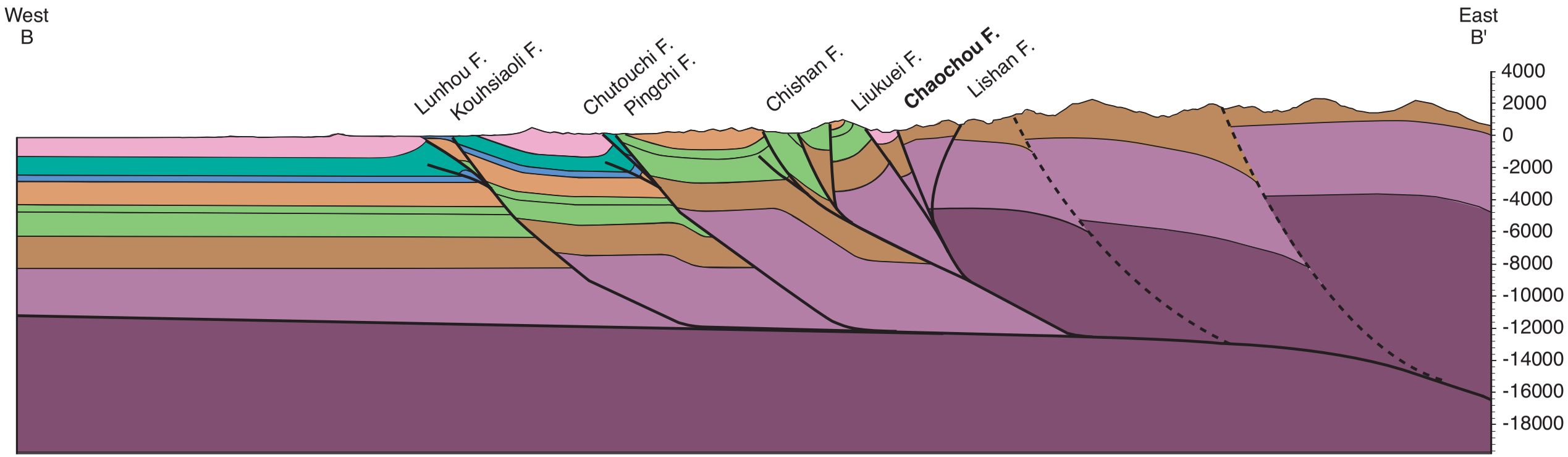

Fig. 7. Line of Section B-B'. Cross sections across the Western Foothills and Slate Belt in Southern Taiwan. Structural and stratagraphic data from CPC geologic maps 6 (Tainan) and 7 (Kaohshiung-Pingtung), and CGS geologic maps 67 (Fanglio) and 51 (Chiahsien), stratigraphic descriptions in Ho, 1989, nearby wells, and one seismic section across the eastern Pingtung Valley by Chang, 1971. No vertical exaggeration.

The Chutouchi and Pingchi faults merge approximately 1 km south of the line of section. Therefore, the Chutouchi fault is, in this interpretation, a minor splay fault to the Pingchi. By our interpretation, the Pingchi fault steepens up-section due to subsequent formation of and displacement on the Kouhsiaoli fault. Displacement accommodated by the Pingchi fault is approximately 5 km.

The Chishan fault accommodates approximately 10 km of displacement. We interpret this fault to be an out of sequence thrust that utilizes east-dipping units in the hanging wall block of the Pingchi fault to cut up section. This line of section cuts across the Western Foothills and CCF in the location of the restraining bend at Liukuei. Out of sequence thrust faulting may result from deformation associated with this restraining bend. We interpret smaller faults in the hanging wall block of the Chishan fault as abandoned thrust faults that have since been passively steepened by uplift and block rotation of units above the Chishan fault.

The Liukuei fault diverges from the CCF 10 km north of line B-B'. To the south, the fault trends into the Pingtung Valley, where it is buried by Quaternary alluvium. The Liukuei fault is interpreted as a precursor to the CCF that exhumed Slate Belt rocks before abandonment and burial by Pleistocene gravels.

The CCF and Lishan faults are drawn with similar geometries as in section A-A'. The basement ramp below the basal detachment is drawn further east to accommodate the approximate 17 km of shortening in the Western Foothills from this interpretation.

1.4.3 Line C-C'

There are few surface data along line C-C' (Fig. 8). It was drawn to incorporate a seismic section from Chang, 1971, on the Pingtung Valley and western Slate Belt margin. The line extends to 3500 m and indicates that Pliocene strata are absent below the eastern Pingtung Valley and that the uppermost units, the Lingkou conglomerate and the Changchikung Formation, thin out to the east. Below the depth of the seismic line, we draw stratigraphy continuing normally and with the same thicknesses as in the two northern cross sections. Absence of the Plio-Pleistocene units may indicate copious

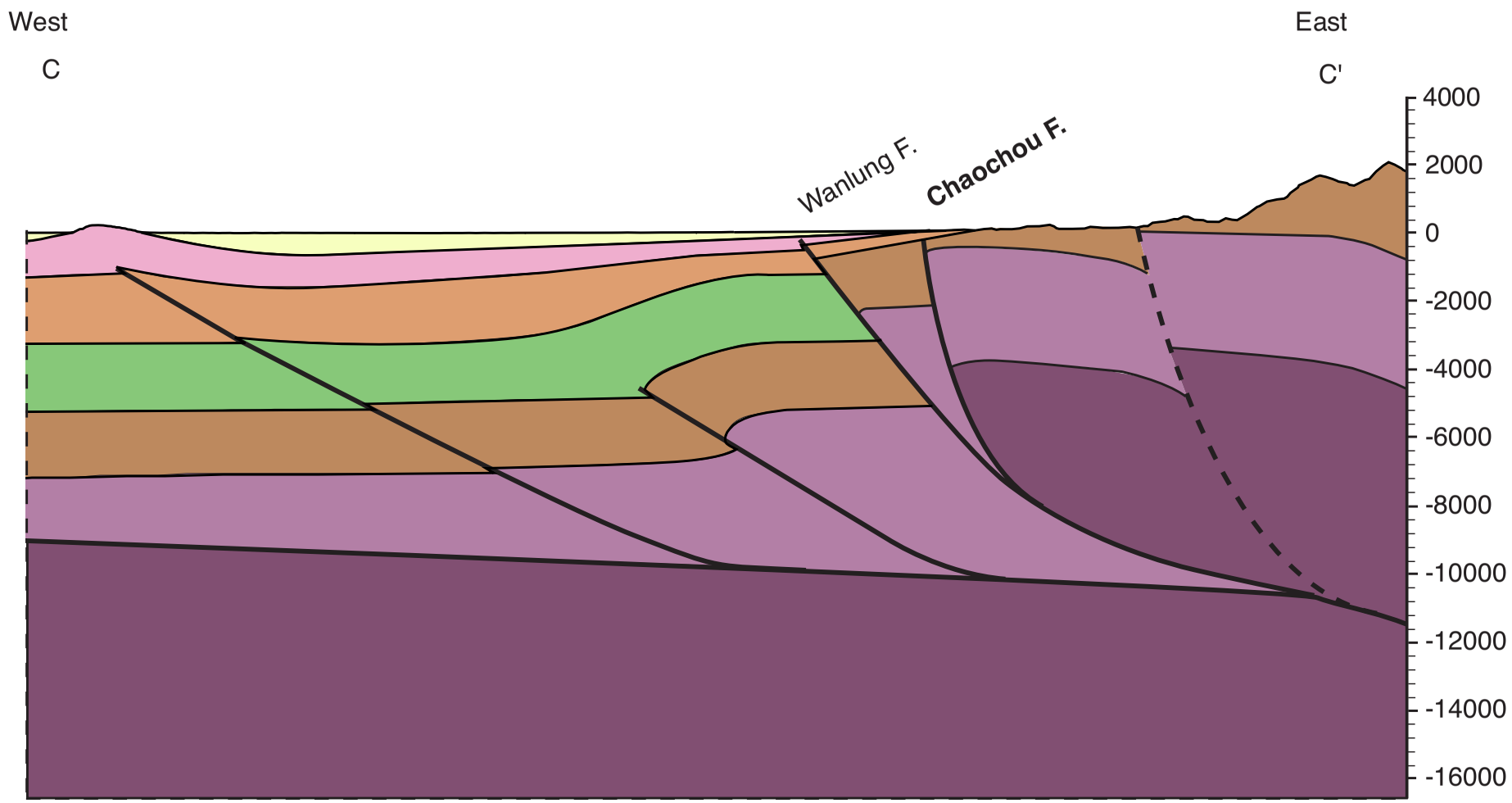

Fig. 8. Line of Section C-C'. Cross sections across the Western Foothills and Slate Belt in Southern Taiwan. Structural and stratagraphic data from CPC geologic maps 6 (Tainan) and 7 (Kaohshiung-Pingtung), and CGS geologic maps 67 (Fanglio) and 51 (Chiahsien), stratigraphic descriptions in Ho, 1989, nearby wells, and one seismic section across the eastern Pingtung Valley by Chang, 1971. No vertical exaggeration.

alluvium was being shed from mountains to the north and east. Alternatively, during that time the valley may have been exposed and has since been down-dropped.

Because the Taiwan orogen is presumably developing southward, we expect structures along the southernmost line of section to have less displacement. We draw a nascent, blind thrust fault from the basal decollement, across the Pingtung Valley, where it forms an anticline at the southernmost extent of the Western Foothills. We draw another blind thrust to account for thinning strata to the east. The Wanlung thrust, imaged in seismic survey (Chang, 1971) is interpreted to be a shallower-dipping precursor to the Chaochou fault carrying Slate Belt rocks. It dips 45 west while the Chaochou fault dips approximately 75 west. Both faults are buried by Quaternary sediments.

2. FABRIC STUDY OF THE SOUTHERN CHAOCHOU FAULT REGION

2.1 Previous Work

Our purpose in examining rock fabric is to document both past motion and deformation related to the CCF and how it changes along strike. The southern extent of fabric characterization in the Slate Belt is the southern Cross Island highway, which runs E-W across the northern portion of the study area. Based on restored vein geometries and syndepositional normal faults from the Slate Belt of central and southern Taiwan, Tillman et al. (1992) identify three distinct extensional regimes, which predate collisional deformation. The direction of extension progressively rotates from NNE-directed to N-directed in the Eocene and Oligocene, and from N to NW-directed during the in the early Miocene. NW extension continued into the middle and late Miocene (Tillman et al., 1992). Some tectonic features of the Taiwan mountain belt may be reactivated extensional structures (Biq, 1989, Deffontaines et al., 1994).

Intensity and complexity of deformation increase eastward across the range. Along the western boundary, strongly asymmetric folds with short and steep to overturned NW limbs and long planar SE limbs are prominent (Clark et al., 1992). These folds show down-dip stretching lineations consistent with flexural slip folding (Tillman and Byrne, 1995). Fold axes trend NNE to NE. The folds are isloclinal to inclined with axial surfaces that dip to the southeast (Tillman and Byrne, 1995). Pressure shadow fibers in these folds are curved and indicate top to the west thrusting and non-coaxial simple shear deformation (Tillman and Byrne, 1995). Second and third phases of folding are distinguished in the eastern portions of the Backbone Range (Clark et al., 1992).

An S_1 solution cleavage, the character of which varies with lithology, is a prominent structural feature of the Slate Belt rocks (Tillman and Byrne, 1995). The S_1 cleavage dips moderately to steeply to the southeast and is axial planar to folds (Tillman and Byrne, 1995). S_1 is typically parallel to bedding and intersects slickenlines on the flexural fold surfaces. This indicates that the development of the solution cleavage

occurred some time after folding and that the observed folds were flattened during development of S_1 (Tillman and Byrne, 1995). Down-dip stretching lineations of the S_1 fabric are consistent with plane-strain deformation (Tillman and Byrne, 1995). Additionally, folds and S_1 cleavage are cut by late late-stage strike-slip faults, conjugate sets that indicate NW-SE shortening (Tillman and Byrne, 1995).

Based on structural relationships, fabric orientations, and zircon fission track annealing ages, Tillman and Byrne, (1996), identify subbelts within the Hsuehshan Range, which indicate that some thrusting within the Slate Belt may have occurred out of sequence from the traditional model of progressive, imbrecating thrusts within an orogenic belt.

2.2 Methods

Field fabric data were collected at 187 locations along the mapped trace of the CCF. Most measurements were taken within 1-2 km of the mapped fault trace. Measurements of foliation, bedding, fold axes, slip surfaces and slip lineations are grouped together into three regions. The northern region is north of the fault bend at Liukuei. The southern region is south of the bend. The middle region is in the fault bend (Fig. 9). The middle region is also the location where the Liukuei and Lishan Faults diverge from the CCF.

2.3 Results

In the northern region bedding and foliation strike NE, nearly parallel to the CCF and dip moderately to the SE; bedding generally dips more steeply to the SE (Fig. 10). It is difficult to distinguish between original bedding and foliation in the northern region. Orientations of bedding and foliation measurements are almost identical and I have decided to combine the bedding and foliation data sets. The equal area plot of combined bedding and foliation data shows two concentrations. The strongest dips moderately to

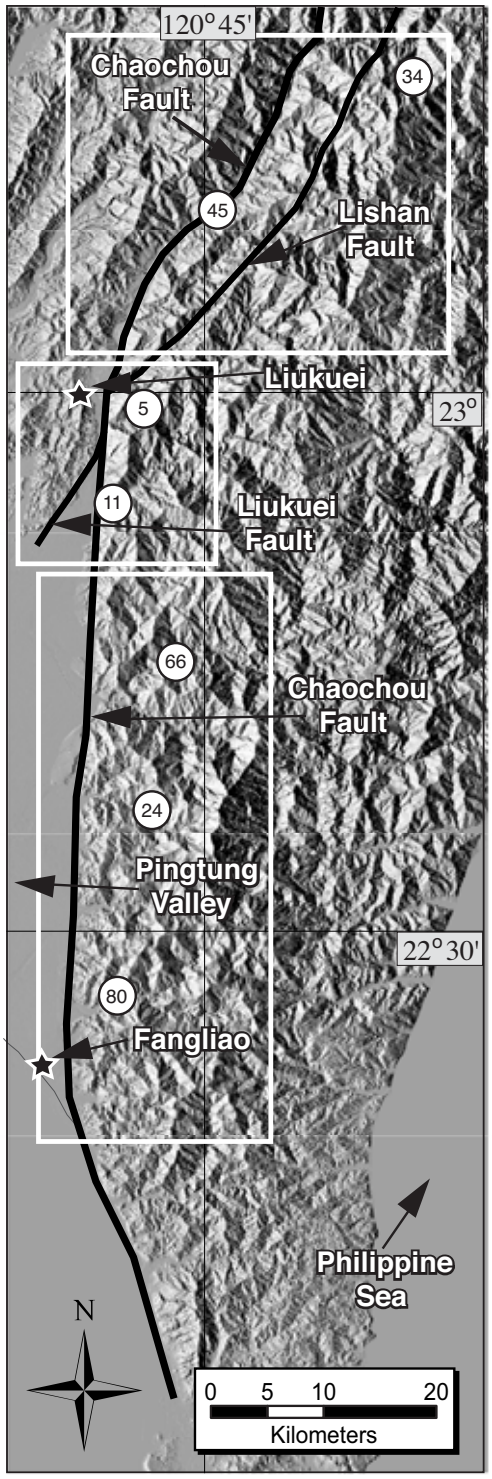

Fig. 9. Digital terrain map of the study area showing the three regions. Prominent geographic and tectonic features are labeled. Sample locations and numbers for XRD analysis are shown as circles.

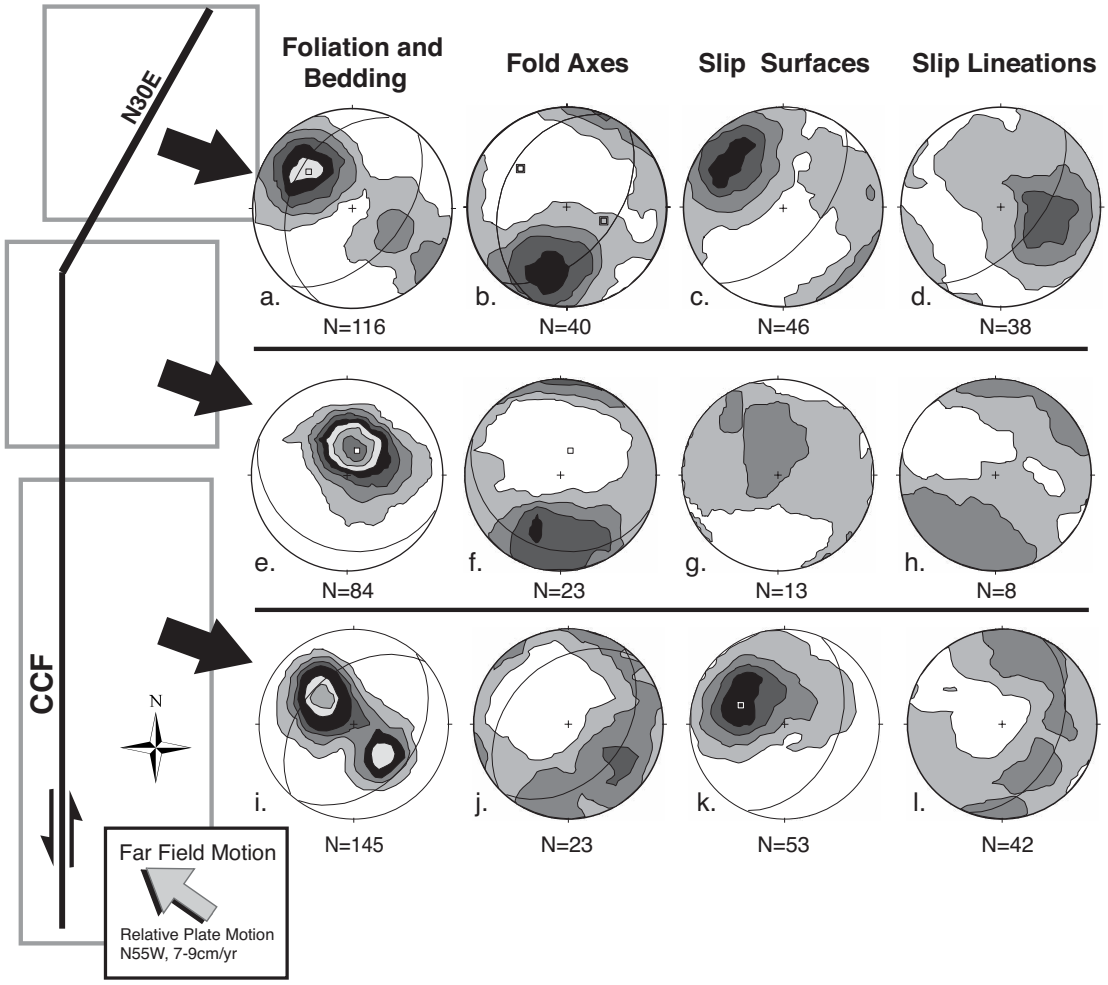

Fig. 10. Field fabric data for the northern, middle, and southern regions. The schematic to the side shows the locations of the regions relative to the CCF. An arrow indicates the relative motion of the Philippine Sea Plate. Plots are lower hemisphere equal area stereograms. Contouring is via modified Kamb method with an interval of 2 Sigma. Significance is set at 3. The number of datapoints is shown below each stereogram.

the SE, and the weaker one to the NW. Both strike NE-SW, parallel to the fault. The two concentrations in foliation orientations probably correspond to the same S_1 and S_2 fabrics described by Tillman and Byrne in the same region, the weaker, north-dipping foliation being the S_2 crenulation cleavage and the stronger southeast-dipping S_1 fabric, a solution cleavage.

Outcrop-scale folds in the northern region are asymmetric, with fold axes plunging gently to the SW. NW-dipping fold limbs are generally short and near vertical, whereas SE-dipping limbs are generally longer and moderately dipping This top to the NW motion is consistent with observations from previous studies (Tillman and Byrne, 1995, 1996; Clark, 1992). Slip surfaces are roughly parallel to the strong foliation direction. Slip lineations (slickenlines and slickenfibers) are concentrated almost directly down-dip of the average slip surface plane. Down-dip slip lineations and foliation-parallel slip surfaces are consistent with observations from previous studies in or near the northern region that indicate folding in the Slate Belt was accommodated by flexural slip along competent bedding planes and by flexural flow in weaker layers (Tillman and Byrne, 1995).

The character of fabrics in the middle region is significantly different from that of the areas to the north and south. Combined bedding and foliation measurements show a single strong preferred orientation, striking WNW, parallel to the CCF, and dipping gently to the SSW (Fig. 10). It is easier to distinguish between bedding and foliation in this section than to the north. However, bedding and foliation still appear to have nearly identical orientations. Fold axes, which represent both folds in bedding and folds in foliation, are oriented approximately N-S, similar to those in the North, but in the Middle region are perpendicular to the strike of foliation. Slip surface and slip lineation data are scarce for this section but show a weak concentration parallel to foliation. Slip lineations were also few, but show a weak down-dip concentration relative to average slip surface orientation.

Two foliation directions in the southern region are similar to those in the north (Fig. 10). As in the northern region, the stronger foliation dips toward the SE and the

weaker one to the NW. Both strike NE-SW, but in the southern region, due to the fault bend, are oblique rather than parallel to the CCF. Slip surfaces are generally parallel to bedding. However, slip lineations do not indicate a preferred orientation of slip, but instead are scattered within the average plane of slip. Many slip surfaces are themselves folded such that the scatter in slip lineations may indicate either flexural slip or post-slip folding.

Fold axes, like in the middle region, are perpendicular to foliation. However, in the southern region they trend NW-SE and plunge toward the SE, unlike fold axes in the middle and Northern regions (Fig. 10). Fold axes in the southern region do not seem to reflect the expected regional shortening direction, NW-SE, nor do they coincide with the expected fold axes direction if the two different foliation orientations are assumed to represent large scale folding. For this reason, the two directions of foliation are not thought to be fold limbs.

2.4 Lithology

Thin sections from rock samples taken along the fault generally show greater strain toward the north. Rocks in the most northeast corner of the northern region, along the Southern Cross-Island highway, comprise mostly pelitic rock subjected to low greenschist facies metamorphism. Veins are concentrated in sandier layers and are typically composed of fibrous quartz and or calcite. Veins are often sheared along grain boundaries; particularly where they cross beds of finer grained material (Fig. 11, A and B). Veins crosscut bedding and predate formation of foliation. Thin sections reveal domainal spaced cleavage characterized by truncated grains (mostly quartz, but occasional micas), and rotated grains (mostly quartz and pyrite framboids) between undulous layers of fine, opaque material. Fibrous quartz fringes are common on large grains and display moderate shear rotation (Fig. 11, E and F). Shear structures indicate top to the northwest shear and are consistent with previously described outcrop-scale

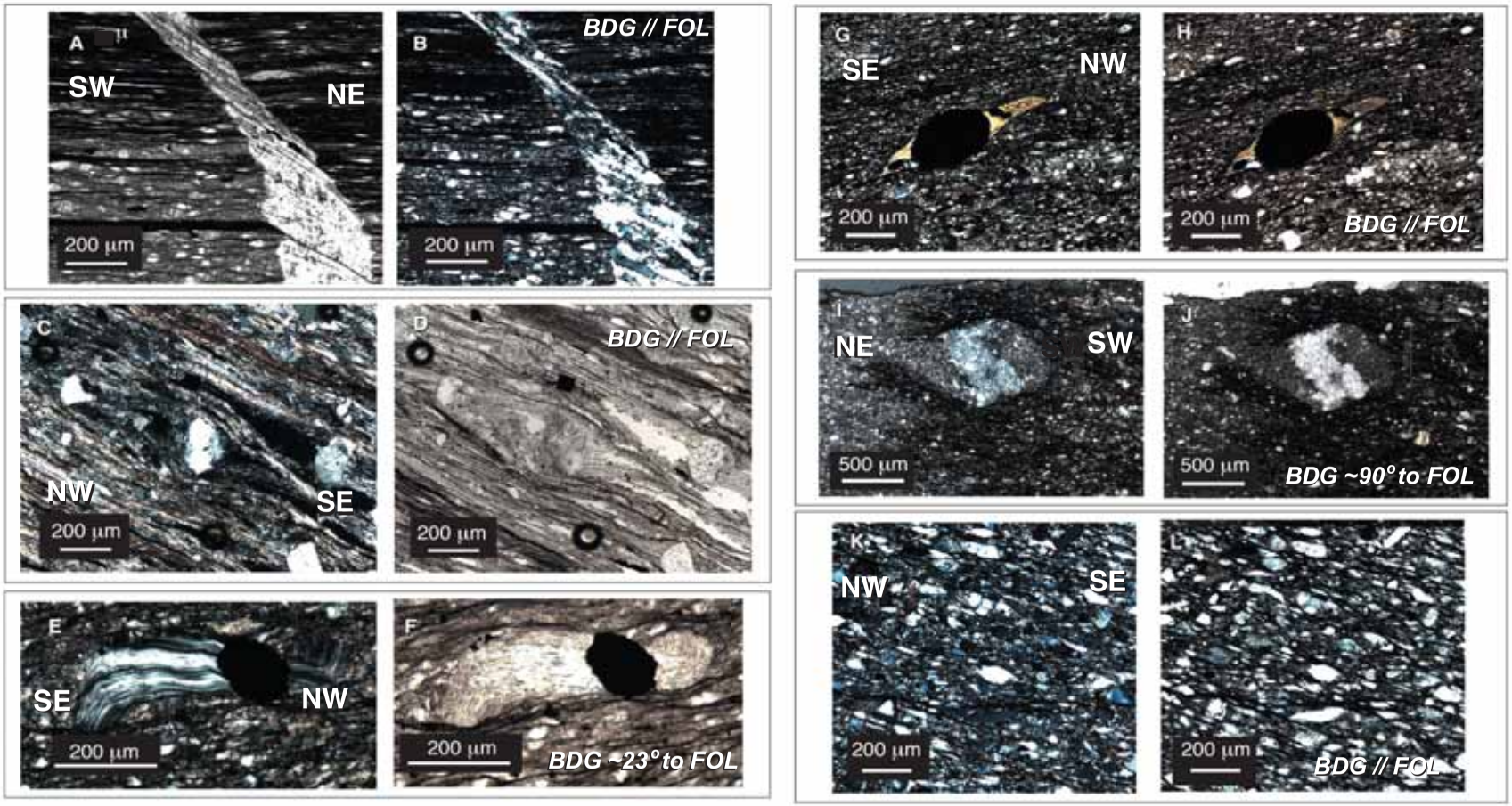

Fig. 11. Photomicrographs showing typical rock fabric and shear structures from Slate Belt rock samples, taken from along the CCF. A-F are from the northernmost portion of the northerny region, along the Southern Cross-Island Highway. A and B show CCW sense of shear; C-F show CW sense of shear. G-J are from the middle region ans show CW sense of shear. K and L are from the southern region. Top is up in each picture. Geographic orientations are shown.

structures. In some instances, shear structures indicate a normal sense of shear (Fig. 11, C and D). These samples are thus interpreted to be found in overturned fold limbs.

Rock lithologies in the middle region comprise similar lithologies to those in the north, but are generally finer grained. Thin sections from samples in the middle region show similar slaty cleavage to those of the north. However, shear structures are much less developed and therefore are difficult to interpret (Fig. 11, G, H, I, and J). Rocks in the south are coarser grained and bedding was easier to distinguish from foliation than is the case with northern and middle units. Solution cleavage is not as strong, though it is still present (Fig 11, K and L). Shear structures were not observed in the south. Absence of shear structures indicates that there has been less simple shearing in this region. Microscale structures indicate a qualitative decrease in strain intensity from north to south.

In rock samples from all study regions, grains large enough to identify in thin section are predominantly quartz and muscovite, with trace grains of microcline, calcite, and pyrite. X-ray diffraction (XRD) patterns on seven samples (see Fig. 9 for sample locations) from along the CCF indicate that the dominant mineralogies in Slate Belt units are quartz and muscovite mica. Diffraction patterns also indicate that the transition from smectite to illite appears to be complete throughout the study area. Ho, (1986) indicates that the western Slate Belt units are prehnite-pumpellyite facies.

3. GEOMORPHOLOGY OF THE SOUTHERN CHAOCHOU FAULT

A key indicator of current motion of the CCF is its tectonic geomorphology. We employed a 40 m Digital Elevation Model (DEM), from which we identified twenty-three major drainages that empty out either onto the Pingtung Plain or into the Laonung River. Stream drainages and drainage divides were manually digitized using the hillshade surface DEM in conjunction with the index contour layer (contour interval 200 m). Major drainage basins were further subdivided into 3rd, 4th, and 5th order basins according to Strahler method (Strahler, 1952).

Large, high order basins can indicate either long-term stability or weak underlying bedrock. The two largest, most mature basins are found just south of the bend at Liukuei (Fig. 12). The occurrence of these two large basins south of the fault bend could indicate that this region has undergone less uplift in recent times. However, we also see that there are no high, 5th-order basins north of the fault bend.

The size and shape of each basin is considered to indicate its maturity or the resistance of the underlying lithology. The larger and more equant the basin and the longer its trunk stream, the more time it has had for both lateral and headward erosion (Burbank and Anderson, 2001). Active mountain fronts will have short, narrow drainage basins that are closely spaced, while inactive fronts will have large, round basins that are also necessarily further apart (Burbank and Anderson, 2001).

Spacing between drainages was examined by measuring the distance of the drainage mouth where it crosses the mountain front, from the southern boundary of the field area (approximately N20 22'). Basin spacing is relatively close in the northern and middle regions and wider in the southern region. Closer spacing indicates higher activity to the north (Fig. 13).

Basin elongation ratio was measured for each of the major drainages along the front by comparing the long axis, which is in most cases roughly perpendicular to the front, following a major stream, to the diameter of a circle having the same area as the given basin (Cannon, 1976).

A.

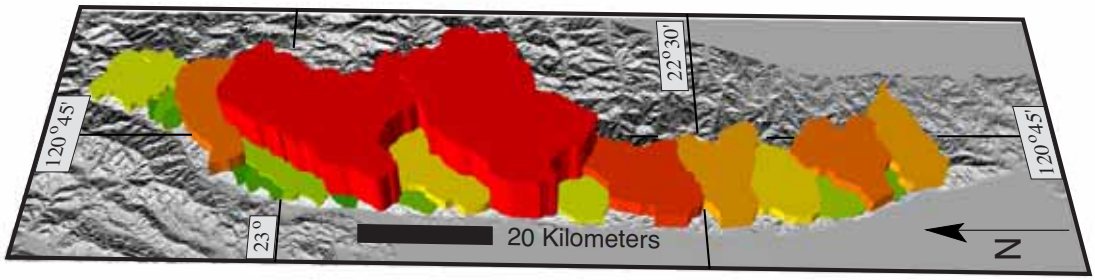

Basin Size

B.

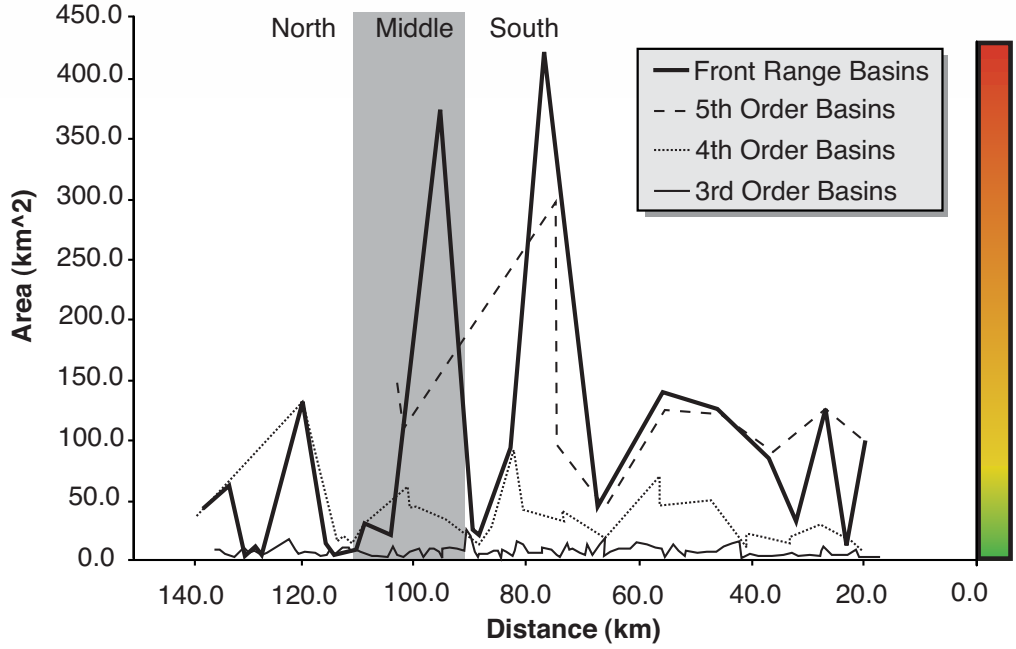

Fig. 12. Basin size. A) Location and size of major range-front drainages along the southern CCF. B) Drainages are further subdivided and classified via Strahler method (Strahler, 1952) into 5th, 4th, and 3rd order basins.

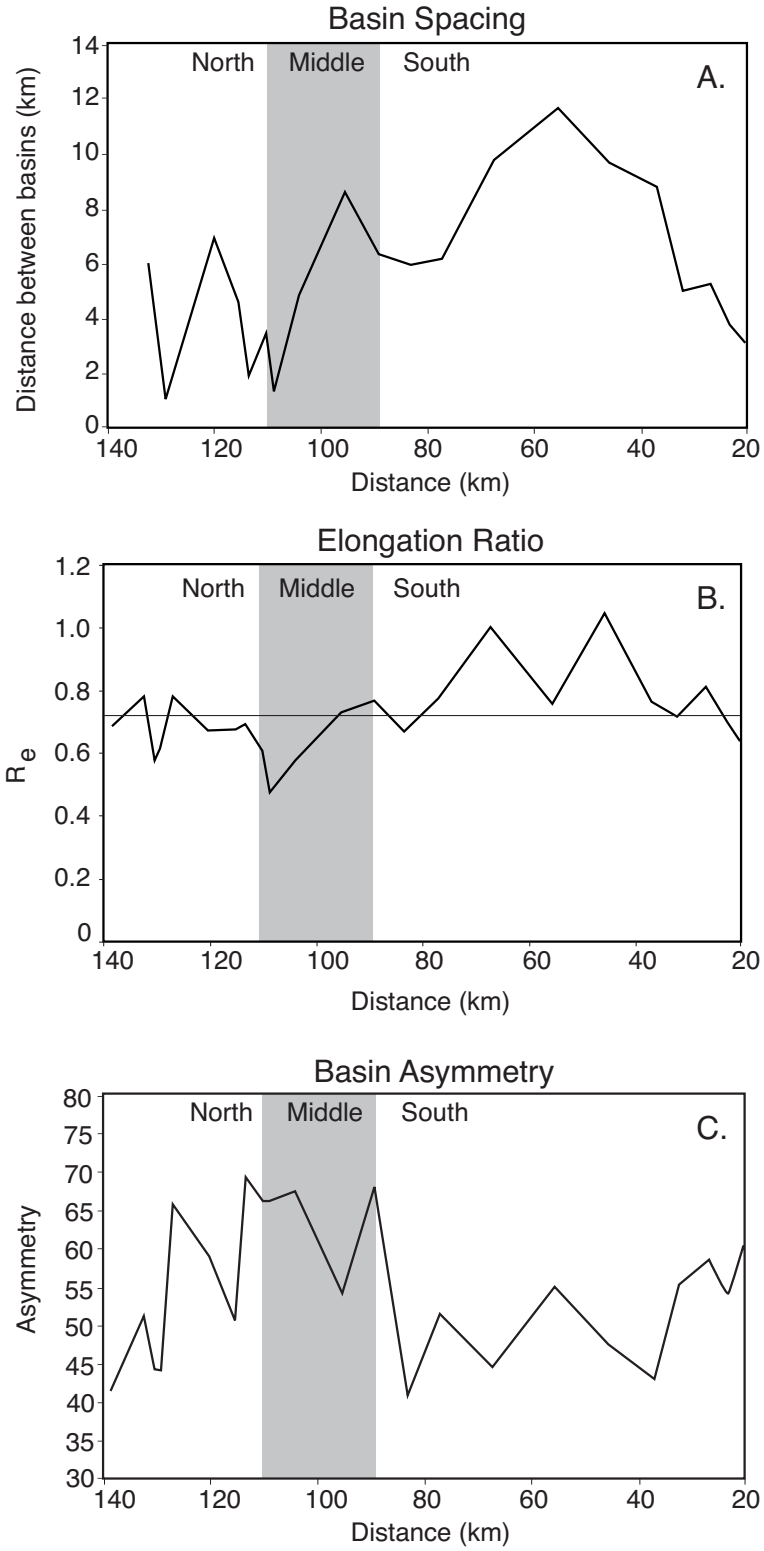

Fig. 13. Drainage basin morphometry. Variations are shown for basin spacing, elongation, and asymmetry along the CCF. See text for equations.

$$R_e = \frac{\text{diameter of circle with the same area as the basin}}{\text{distance between the two most distant points in basin}} \qquad (1)$$

Basin shape will affect the spacing of drainages along the front. Major basins tend to be more elongate in the northern and middle regions, and more round in the southern region. Basin elongation correlates with basin spacing because more elongate streams allow for closer spacing (Fig. 13).

Basin asymmetry is determined by following the main trunk stream up until it branches into to lower-order streams. From there the midline becomes the drainage divide between the two sub basins. The drainage basin asymmetry factor (A_s) was determined by calculating the area of the basin on the right side of the midline (A_r, facing down-stream). That area was then calculated as a percentage of the total basin area (A_t) as defined in Hare and Gardener (1985):

$$A_s = 100 * \left(\frac{Ar}{At} \right) \qquad (2)$$

Those basins for which the A_s is less than 50 percent are tilted relatively to the left, and for those which the A_s is greater than 50 percent are tilted relatively to the right. Asymmetry must be compared among basins whose trunk streams are all similarly oriented (Keller and Pinter, 2002). Streams in the middle region may be tilted slightly toward the south (Fig. 13). Strong, southeast-dipping foliation may also account for the appearance of southward tilting.

Stream gradient plotted along the length of the major trunk streams for each basin reveals that the overall stream gradient is higher in the northern region (Fig. 14). This is expected as basins in the north are generally smaller and at a higher elevation. Two streams occur in the northern regions in which the gradient increases very rapidly in the middle of their lengths. The occurrence of these increases in stream gradient could indicate that the frontal CCF recently underwent active uplift, the affects of which are propagating back along the streams as knickpoints. Knickpoints are generated where

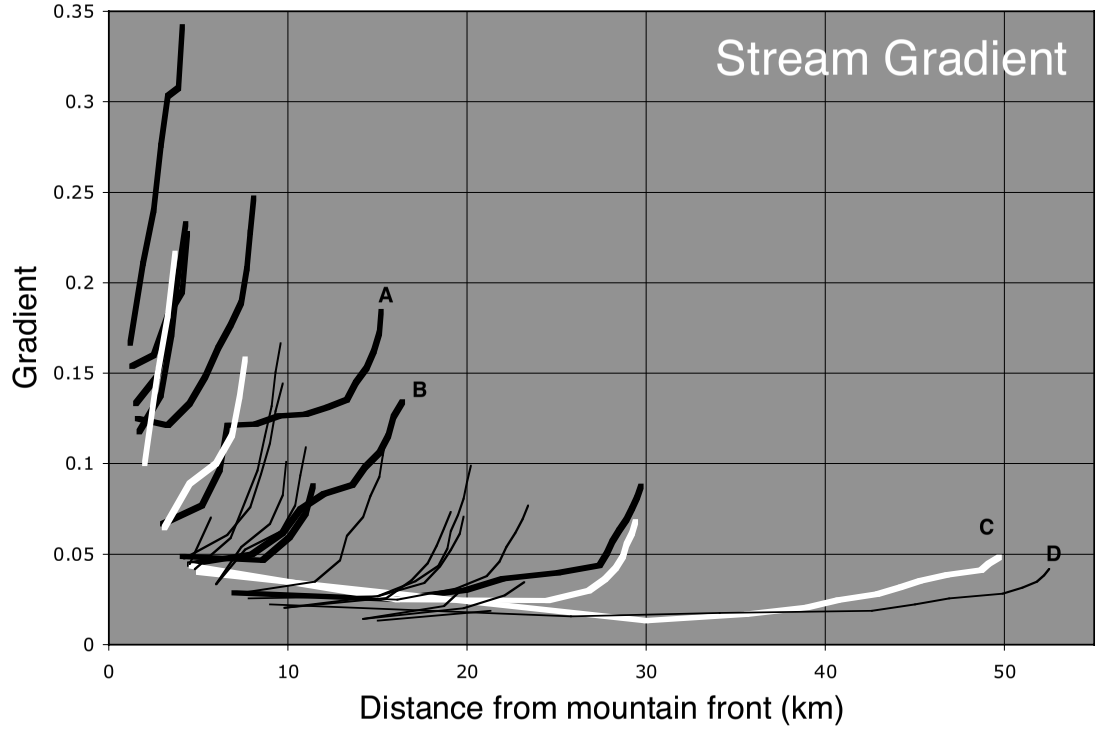

Fig. 14. Plot of stream gradient vs. distance from the mountain front for major drainages. Heavy black lines = northern region streams, heavy white lines = middle region streams, thin black lines = southern region streams. Two northern streams (A and B) show obvious knickpoints in their middle reaches. The two largest drainages (C and D) have a steeper gradient near their mouths than in their middle reaches.

baselevel lowers faster than the stream can erode, and can propagate upstream great distances from their source, especially in rivers that are incising bedrock (e.g. Ritter et al., 2002). However, that source may not necessarily be located at the mouth of the stream (Ritter et al., 2002). The knickpoints observed in this study may also indicate that the streams cross over an active subsidiary to the CCF.

The gradient profile for the two largest drainages, one of which empties into a large entrenched alluvial fan, is concave upward and indicates the stream is not at equilibrium with uplift and/or climate conditions. Uplift or folding at the mouths of these drainages, or a rapid increase in sediment supply could produce a concave up profile. Increased uplift at the mouth, does not favor alluvial fan entrenchment, which is observed in this area (discussed below). Sediment supply naturally increases as a function of upstream basin area. As these are by far the largest basins in the study area, their size may account for the abundance of sediment. Other catastrophic events, such as heavy rainfall that triggers mudslides or stream piracy at the headwaters could account for increased sediment fluxes at the mouths of these drainages. Alternatively, rapid uplift and steepening in the interior of the range would increase stream power and therefore sediment supply. It is more likely that increased sediment supply is responsible for the observed concave up gradient profiles. However, further study is needed to determine the factors controlling this increase.

The large entrenched alluvial fan found at the mouth of northernmost of the two largest drainage basins may indicate either a lessening of tectonic uplift, or a Holocene climate change from dry to more humid conditions. Entrenched alluvial fans are characteristic of a moderately active mountain front (e.g. Bull and McFadden, 1977). Stream incision often implies a change in local or regional base level. The mountain belt may experience uplift and thus foster rapid down cutting of a stream by steepening the channel and increasing stream power. Contrary to these observations, entrenched alluvial fans imply a lessening of uplift through time, particularly uplift at the mountain front. As uplift slows to below the rate of downcutting, deposition migrates from the apex of the alluvial fan outward and entrenchment occurs as the stream equilibrates (Bull, 1977).

In addition to tectonic controls, alluvial fan entrenchment may also be initiated by sea level fluctuations, climate change, or changing sediment supply. Marine regression, such as that observed since 8-6 ka, lowers base level and favors incision. Climate change from humid to dry conditions decreases vegetation, thereby increasing weathering on slopes. This leads to increased sediment supply and aggradation of alluvial deposits. Climate change from dry to humid conditions has the opposite effect. More vegetation decreases surface weathering and sediment supply while increasing stream discharge, thereby promoting erosion of alluvial deposits. Recent studies of pollen spores from southern Taiwan indicate dryer conditions may have occurred existed before 13 and 10 ka, and have subsequently become more humid (Sung et al., 1997).

The valley floor width to valley height ratio (Bull and McFadden, 1977),

$$V_f = \frac{V_{fw}}{\frac{(E_{ld} - E_{sc}) + (E_{rd} - E_{sc})}{2}} \qquad (3)$$

compares the width of a stream valley to its height. Small ratios indicate narrow valleys with high walls, whereas high ratios indicate broad stream valleys whose width is significantly greater than the valley height. These measurements are made along front parallel transects of the stream valleys between 2 and 5 km east of the mountain front using the profile tool in ArcGIS to create the valley profile. Along this transect, the elevations of the stream (E_{sc}), the left and right drainage divides (E_{ld}, E_{rd}), and the valley floor width (V_{fw}) were measured. Smaller drainages have less stream power with which to downcut. As a result, smaller streams will tend to have a lower Vf value (meaning a stronger V-shape rather than a broad flat valley) than will larger streams operating in the same tectonic regime. The northern and middle lengths of the mountain front are characterized by narrow, steep valleys, and indicate rapid recent uplift along the front (Fig. 15 A). Larger ratios in the south indicate broad valleys that have had time to incise the mountain front as well as eroding laterally.

Mountain Front Sinuosity (S_{mf}) is used as a proxy for mountain front activity. The mountain front was described by manually digitizing the slope break, set where slope increased/varied by one standard deviation across slope of the Laonung River valley and Pingtung Valley and into the Slate Belt. To determine mountain front sinuosity ($S_{mf)}$, the actual total length (L_t) of the front and the straight-line length (L_s or distance made good, D_{MG}) were calculated (Dan Rathert, personal communication). Sinuosity:

$$S_{mf} = \frac{L_{mf}}{L_s} = \frac{L_t}{D_{MG}} \qquad (4)$$

was then calculated with the total length (or length of mountain front, L_{mf}) and the D_{MG} (Bull and McFadden, 1977). Using this equation, the longer the total length of the mountain front is relative to the straight-line length, the greater the sinuosity. A high sinuosity is thought to be related to, 1) a less active front for which stream erosion and embayment occurs faster than uplift along the fault, or 2) to the presence of a weaker lithology in which downcutting and erosion occurs more quickly than in a more resistance bedrock (Bull and McFadden, 1977; among many others). Sinuosity is expected to be higher where basins are closely spaced. Narrow, elongate basins denote rapid uplift and subsequent downcutting of the stream, and allow for closer spaced drainages and increased sinuosity. This may give the appearance of slower uplift rates along the front.

The mountain front was split into segments of equal length to evaluate changes in sinuosity along the mountain front. Length intervals of approximately five, ten, and twenty kilometers were used to assess the effect of line segment length on sinuosity (Fig. 15 B). The different line lengths yield similar trends. However, the shorter segment lengths are more sensitive to the local effects of stream drainages along the mountain front. Mountain Front Sinuosity (S_{mf}) along the CCF is much lower north of the fault bend at Liukuei and is lowest just south of the bend. Sinuosity values correlate well with

valley floor width/height ratios of stream valley profiles and indicate less activity along the front to the south (Fig. 15).

Taken together, the geomorphological measures indicate that the northern and middle regions have been more recently active than the southern region. Basins in the north tend to be smaller and of a lower order. The morphology of northern and middle region basins is more elongate and they are closer spaced. Stream gradients are higher in the northern and middle regions. In addition to stream and basin parameters, mountain front morphology also suggests more recent activity in the north and middle regions. Values of both V_f and S_{mf} are lowest in the north, particularly at the fault bend near Liukuei.

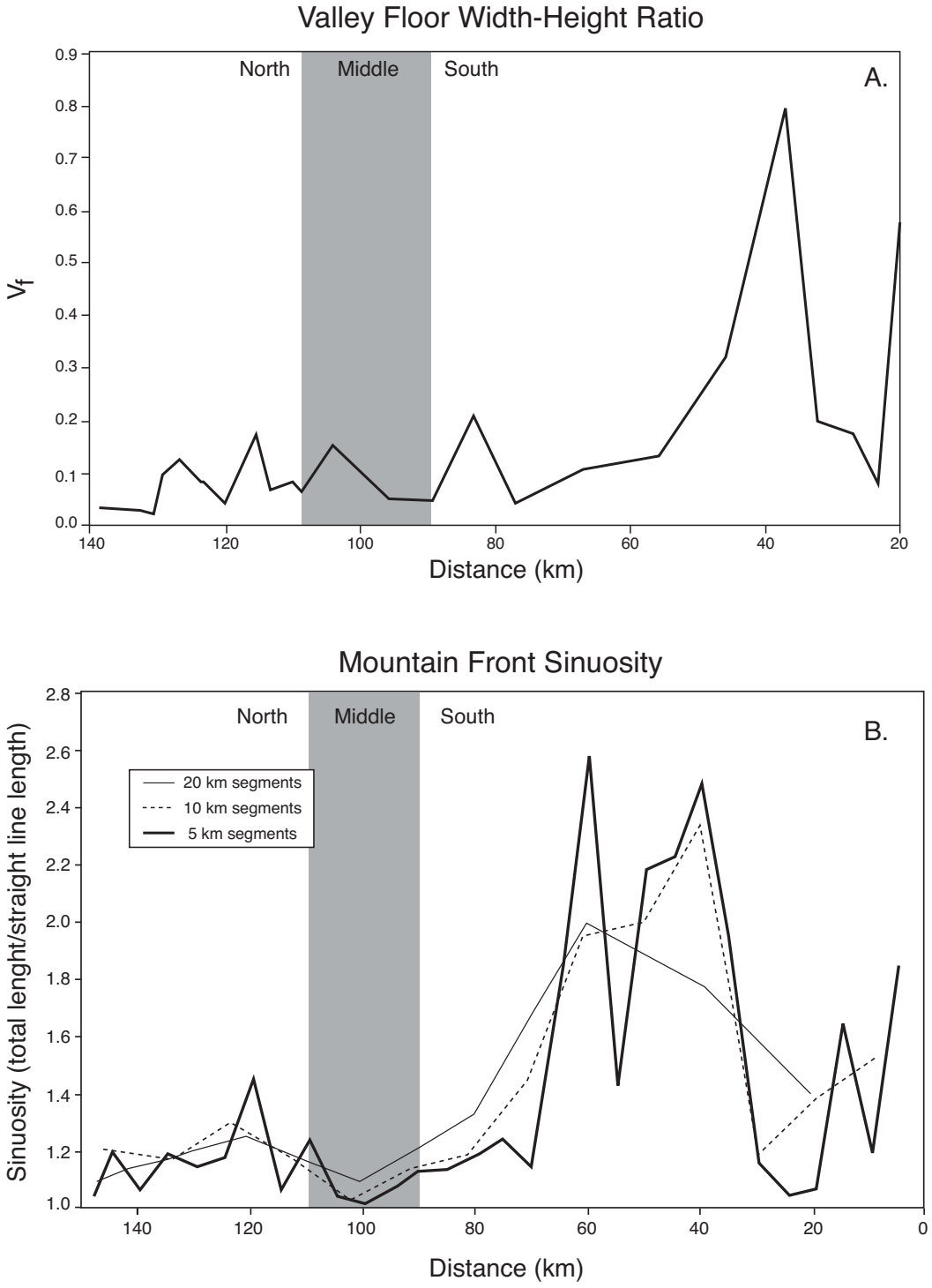

Fig. 15. Variations in mountain front parameters. Vf (A.) and Smf (B.) are shown vs. distance. Lower values for both parameters indicate higher activity in the northern and middle regions.

4. DISCUSSION

Our data indicate that activity along the CCF increases to the north and is consistent with a southward-developing orogen. The northern and middle regions are active and have been for some time, while the southern region appears to be less active and at a younger stage of development relative to the north.

The northern and middle regions have the highest current uplift rates based on GPS data. Geomorphic parameters indicate that the northern and middle regions have undergone recent uplift as indicated by elongate, closely spaced basins, steep stream gradients, high S_{mf}, and low V_f values (Figs. 13, 14, and 15). Younger apatite and zircon fission track ages indicate that rocks in the northern and middle regions are exhumed from greater depth than those in the south and that the orogen is more mature in the north. Quartz fringes in the north show greater rotation than those in the middle region (Fig. 11). Fabric orientations in the northern region suggest NW-SE-directed shortening that are colinear with the far-field stress direction inferred from the NW motion of the Philippine Sea Plate (Fig. 10). Inferred shortening orientations for brittle and ductile fabrics do not coincide in the middle and southern regions. Fabric orientations change abruptly in the middle region, perhaps due to fault block rotation. Two faults diverge from the CCF in this region and may be responsible for late-stage reorientation of preexisting fabric.

Fabric orientations in the southern region are different from those in the northern and middle regions, though foliation orientations are similar to those in the north. The southern region is tectonically younger than the north and represents a shallower portion of the accretionary wedge. Because brittle and ductile fabrics do not indicate the same direction of compressive stress, as is the case in the middle region, this may indicate either that the stress state changes with depth or that rocks in the western Slate Belt are rotated as they are brought up from depth. The actual transition between the different fabric orientation seen throughout the different study regions occurs

abruptly between the northern and middle regions, at approximately 23.1 N latitude, and is more gradational between the middle and southern regions.

GPS surface motion data show variation in current surface deformation along the CCF. Present motion along the CCF is not well constrained because GPS data are sparse within the Slate Belt and Central Range. However, it is clear that there is some deflection of surface motion vectors across the fault. When surface motions are calculated relative to the Philippine Sea Plate, vectors rotate southward traversing the island from west to east (Fig. 16, Wiltschko et al., 2002). North of the fault bend, motion vectors trend toward the southeast. South of the bend they trend due almost due south. The magnitude of vertical motion also decreases across the fault. When surface motions are calculated relative to sites along the CCF, motion vectors east of the fault trend toward the NW, whereas east of the fault velocity vectors trend mostly due west. Vertical velocity data from GPS indicate that uplift rates vary along the fault. Greatest uplift rates occur in the northern region on both sides of the CCF. Uplift is negligible to the south.

In addition to current deformation, long term uplift from apatite/zircon fission track ages also indicates more active uplift to the north. Liu et al. (2001) observed that zircon and apatite fission track ages generally increase from east to west, traversing the island, and indicate that greatest uplift occurs at the collisional boundary and decreases with increasing distance. Liu et al (2001) observed that the occurrence of reset units decreases to the south where the orogen is presumed to be younger. Fuller (2003) found that young reset ages become similar to the north, indicating that the orogen has achieved steady state approximately 80 to 130 km from the southern tip of the island.

Fuller (2003) notes a repeat in the progression from reset to unrest ages across the Hsuehshan Range. This range may expose rocks from more shallow portions of the deformation wedge. Reset ages indicate higher uplift rates in central Taiwan, well west of the plate boundary. The Peikang High basement anomaly may influence uplift rates in this region by acting as an indentor (Liu et al., 2001).

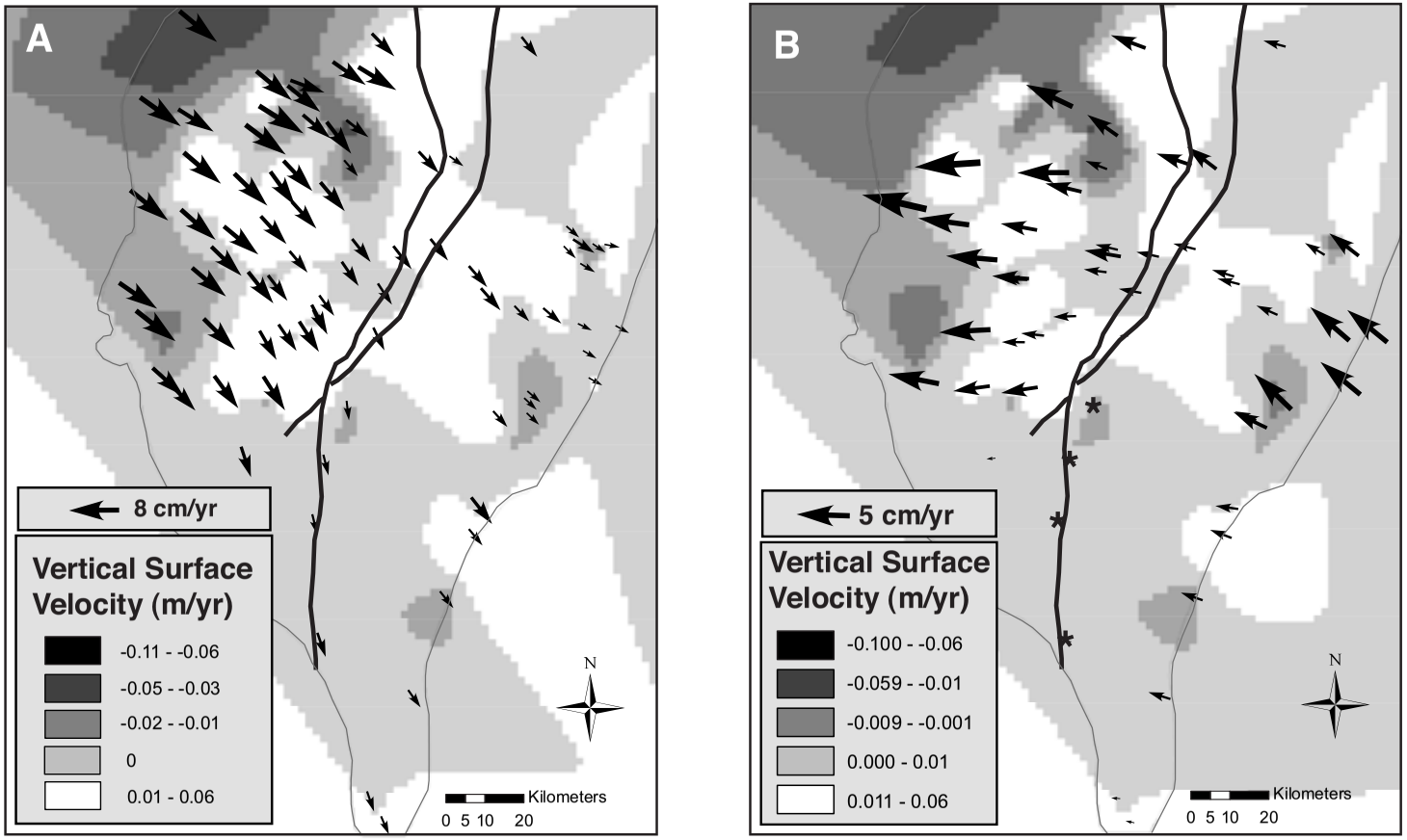

Fig. 16. GPS surface motion data for southern Taiwan. Contours represent vertical velocity. Black arrows represent horizontal motion velocity vectors. A) Surface deformation rates relative to the Philippine Sea Plate. B) Deformation rates relative to GPS sites along the CCF (marked with *'s).

In the northern region, fission track ages from samples adjacent to the fault are un-reset and indicate that the rock is uplifted from shallower depth than those directly east and south (Fig. 17). How far these older, un-reset ages extend eastward into the Slate Belt is not known. The southern-most tip of the Hsuehshan Range extends down into the northern region and may be responsible for the region of unreset units.

Fission track ages adjacent to the fault in the region of the bend are young and suggest uplift and exhumation from a deeper portion of the orogen and perhaps more rapid uplift along this segment. This could be due to the influence of the Peikang High indentor or the presence of the restraining bend, or possibly both as the Peikang High may be responsible for the development of the restraining bend (Biq, 1989).

Moving southward, fission track ages change from younger, reset ages to intermediate ages toward the south (Fig. 17). Fission track ages in the southern region indicate unreset strata. The younger ages in the southernmost Hengchun Peninsula are interpreted to have been reset upon deep burial within the accretionary wedge rather than exhumed, basement material (Fuller, 2003).

Fission track ages tell a slightly different story than the GPS surface velocity data. While the northern region appears to be most active today, fission track data indicate that the middle region, where the lowest track ages are found directly adjacent to the fault, has seen the most uplift. Both current and long-term data suggest that the southern CCF has experienced slower uplift than regions to the north.

Seismic data further support a change in the amount and style of active deformation in southern Taiwan. Beneath southern Taiwan, the Chuchi Transfer Fault Zone (CTFZ) cuts across the island at high angle to the regional structural trend of the island (Fig. 1, Lacombe et al., 2001, Lallemand et al., 2001). The CTFZ, recognized primarily by seismicity, is thought to be a precollisional basement transform fault that has since been reactivated, perhaps by collision with the Peikang High (Lacombe et al., 2001). South of the CTFZ, the number of seismic events falls off sharply (Lacombe et al., 2001, Teng et al., 2000).

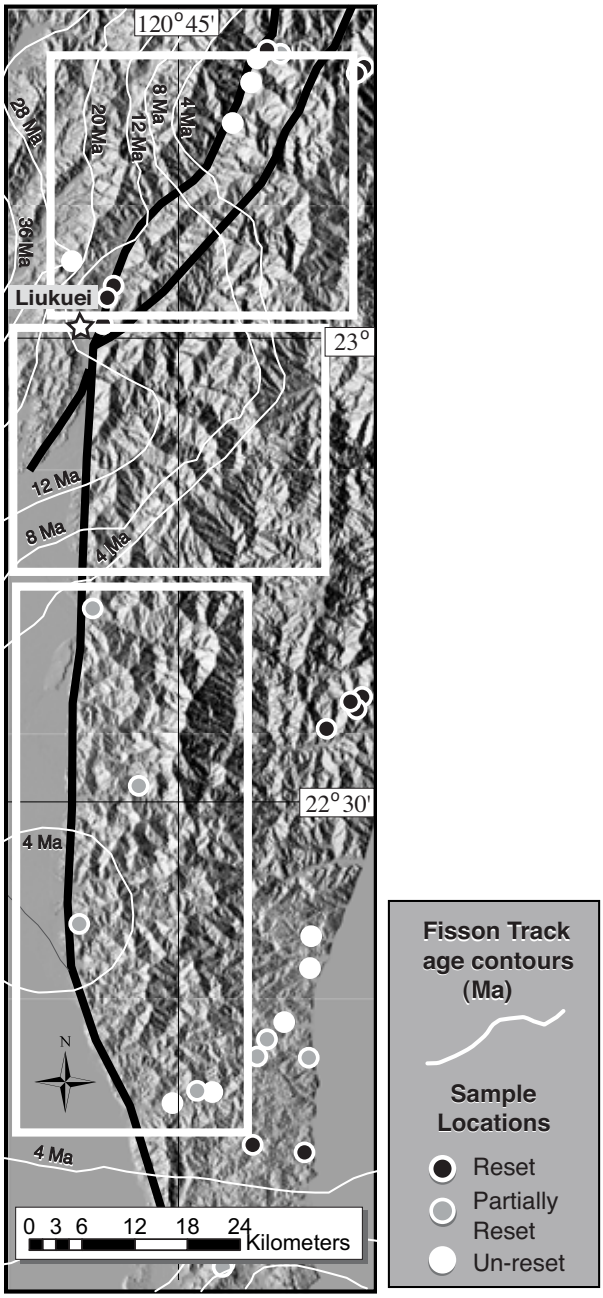

Fig. 17. Zircon/Apatite fission track ages. Ages are contoured and sample locations are indicated with colored circles. As in previous studies, samples are designated as totally reset, unrest, and partially reset when they are significantly younger than the stratigraphic age of the host rock (<6 Ma, in Taiwan), significantly older than the host (>90), or intermediate between those two end members (10-100 Ma), respectively (Liu et al., 2001, Fuller, 2003, Willet et al., 2003).Note the youngest samples are found near Liukuei. Ages increase to the south. Data from Fuller, 2003.

The Liukuei region also appears to mark a significant change in the character of focal mechanisms in southern Taiwan (Lacombe et al., 2001). In the east, compression axes are nearly parallel to plate motion, while in the southwest they have rotated to NE-SW, almost 90 degrees from relative plate motion (Yeh et al., 1991). The change occurs somewhere in the vicinity of the Pingtung Valley/CCF. The exact mechanism for the change is unclear. Lacombe et al., (2001) suspect that the region south of the CTFZ is the on-land extension of the Manila trench accretionary prism, which is forming via collision with the South China Sea and the PSP; to the north lies the arc-continent collision between the Luzon Arc and the Eurasian continental margin.

The on-land location of the continent ocean boundary (COB) is not known. It may form the eastern boundary of the Pingtung Valley and thus intersect the western Central Range and CCF near the fault bend at Liukuei (Wiltschko, personal communication). A sharp change in lithospheric strength or bouyancy such as that at a continent ocean boundary could explain the change in character of seismicity seen in southern Taiwan, and may account for other observed changes in rock fabric orientations and increasing activity and uplift of the CCF in the region of the Liukuei fault bend.

5. CONCLUSIONS

This study has shown, through examination of rock fabric and mineralogy, surface morphology, and current surface motion, that activity of the Chaochou Fault and Slate Belt increases northward within our study area. These observations are consistent with a southwardly younging mountain belt. Here we summarize the conclusions and implications put forth in this study.

1) Fabric orientations change abruptly along strike of the CCF. These changes in orientation may reflect local rotation of fault blocks bound by unmapped subsidiaries to the CCF, changes in lithology, or prior changes in stress conditions at depth that are exposed due to differential uplift along the fault.
2) Micro-scale rock fabric indicates qualitatively that the intensity of strain decreases to the south. This likely reflects that the orogen is developing to the south and therefore, from north to south, exposed units are progressively younger and represent a shallower portion of the orogenic wedge.
3) Surface morphology indicates more recently active uplift in the northern and middle study areas, particularly at the mountain front at the restraining bend near Liukuei.
4) GPS vertical surface motion data indicate more rapid uplift in the north. Horizontal velocity vectors rotate clockwise along strike of, and are deflected across the CCF.
5) It is likely that the changeover from direct arc-continent, to ocean-arc collision and accretionary wedge formation occurs near the bend at Liukuei. Observed changes in lithology, deformation and rock fabric, surface morphology, and surface motion support this conclusion. In addition, the presence of the Peikang High indentor to the north may also influence deformation, causing higher uplift in the northern and middle regions.

Future work in this complex and fascinating region should include efforts to install a denser geodetic network in the Central Range, which would allow for greater resolution of current fault motion. Completion of detailed mapping in the Slate Belt and Central Range will greatly improve our understanding of the structure of that region. Also, more subsurface data is crucial for accuracy in resolving geometry and timing of development of the Chaochou Fault and the Taiwan mountain belt.

REFERENCES

Anczkiewicz R., Burg J.P., Villa I.M., and Meier, M., 2000. Late Cretaceous blueschist metamorphism in the Indus Suture Zone, Shangla region, Pakistan Himalaya. Tectonophysics 324, 111-134.

Biq, C., 1989. The Yushan-Hsüehshan megashear zone in Taiwan. Geol. Soc. China 32, 7-20.

Brown D, Alvarez-Marron J, Perez-Estaun A, Puchkov V, Gorozhanina Y, and Ayarza P., 2001. Structure and evolution of the Magnitogorsk forearc basin: Identifying upper crustal processes during arc-continent collision in the southern Urals. Tectonics 20 (3), 364-375.

Bull, W.B., 1977. The alluvial fan environment. Progress in Physical Geography 1, 222-270.

Bull, W.B. and McFadden, L.D., 1977. Tectonic geomorphology north and south of the Garlock Fault, California. In: Doehring, D.O, (Ed.). Geomorphology in Arid Regions. Allen & Unwin, London, 272 pp.

Burbank, D.W., and Anderson, R.S., 2001. "Chapter 10: Tectonic Geomorphology at Intermediate Time Scales." In: Burbank, D.W., and Anderson, R.S. (Ed.), Tectonic Geomorphology. Blackwell, Malden, Massechusetts, pp. 201-230.

Cannon, P.J., 1976. Generation of explicit parameters for a quantitative geomorphic study of the Mill Creek drainage basin. In: Oklahoma Geology Notes, v. 36, 3-16.

Central Geologic Survey (CGS), MOEA, 1993. Geologic map of Taiwan, Sheet 67, Fangliao. Tunyow Huang (Dir.). Scale 1:50,000, 1 sheet.

Central Geologic Survey (CGS), MOEA, 2000. Geologic map of Taiwan, Sheet 51, Chiahsien. Chao-Hsia Chen (Dir.). Scale 1:50,000. 1 sheet.

Chang, S.C., 1971. Seismic study of the Chaochou structure, Pingtung, Taiwan. Petroleum Geology of Taiwan 8, 281-294.

Chen, Y.C., Sung. Q., and Cheng, K.Y., 2003. Along-strike variations of morphotectonic features in the Western Foothills of Taiwan: tectonic implications based on stream-gradient and hypsometric analysis. Geomorphology 56, 109-137.

Chiang, S.C., 1971. Seismic Study of the Chaochou Structure, Pingtung, Taiwan. Petroleum Geology of Taiwan 8, 281-294.

Chinese Petroleum Corporation (CPC), 1989. Geologic map of western Taiwan, No. 6, Tainan Sheet. Taiwan Petroleum Exploration Division (TPED), scale 1:100,000, 1 sheet.

Chinese Petroleum Corporation (CPC), 1992. Geologic map of southern Taiwan, Sheet 7, Kaohshiung-Pingtung sheet. Taiwan Petroleum Exploration Division (TPED), scale 1:100,000, 1 sheet.

Clark, M.B., Fisher, D.M., and Lu, C.Y., 1992. Strain variations in the Eocene and older rocks exposed along the central and southern cross-island highways, Taiwan. Acta Geologica Taiwanica 30, 1-10.

Deffontaines, B., Lee, J.C., Angellier, J., Carvalho, J., and Rudant, J.P., 1994. New geomorphic data on the active Taiwan orogen: a mulitsource approach. JGR, 99, B10, 20,243-20,266.

Delcaillau, B., Deffontaines, B., Floissac, L., Angelier, J., Deramond, J., Souquet, P., Chu, H.T., and Lee, J.F., 1998. Morphotectonic evidence from lateral propagation of an active frontal fold; Pakuashan anticline, foothills of Taiwan. Geomorphology 24, 263-290.

Ernst, W.G. and Harnish, D., 1983. Mineralogy of some Tananao Greenschist facies rocks, Mu-Kua Chi area, eastern Taiwan. Preceedings of the Geological Society of China 26, 99-112.

Fuh S.C., Liu C.S., Lundberg N., and Reed D.L., 1997. Strike-slip faults offshore southern Taiwan: Implications for the oblique arc continent collision processes. Tectonophysics 274 (1-3), 25-39.

Fuller, C.W., 2003. Thermochronometry and Thermomechanical Modeling of the Taiwan Orogen. Master's Thesis, U. of Washington, Seattle, 82 pp.

Hare, P.W., and Gardner, T.W., 1985. Geomorphic indicators of vertical neotectonism along converging plate margins, Nicoya Peninsula, Costa Rica. In M. Morisawa and Hack, J.T. (eds.), Tectonic Geomorphology: Preceedings of the 15th Annual Binghamton Geomorphology Sumposium, September 1984. Allen and Unwin, Boston, pp. 75-104.

Hickman J.B., Wiltschko, D.V., Hung, J.H., Fang, P.F., and Bock, Y., 2002. Structure and evolution of the active fold-and-thrust belt of southwestern Taiwan from GPS analysis. In GSA Special Paper 358, 79-96.

Ho, C.S., 1986, Geological Map of Taiwan. Cent. Geol. Surv., MOEA, Taipei. Scale 1:500,000, 1 sheet.

Kao, H., and Jian, P.R., 2001. Seismogenic patterns in the Taiwan region: insights from source parameter inversion of BATS data. Tectonophysics 333, 179-198.

Keller, E.A. and Pinter, N., 2002. Active Tectonics: Earthquakes, Uplift, and Landscape. 2nd ed. Prentice Hall, Upper Saddle River, New Jersey, 362 pp.

Lacombe, O., Mouthereau, F., Angelier, J., and Deffontaines, B., 2001. Structural, geodetic, and seismological evidence for tectonic escape in SW Taiwan. Tectonophysics 333, 323-345.

Lallemand, S., Font, Y., Bijwaard, H., and Kao, H., 2001. New insights on 3-D plates interaction near Taiwan from tomography and tectonic implications. Tectonophysics 335, 229-253.

Lee, J.C., Angelier, J., and Chu, H.T., 1997. Polyphase history and kinematics of a complex major fault zone in the northern Taiwan mountain belt: the Lishan Fault. Tectonophysics 274, 97-115.

Liu, C.S., Huang I.L., and Teng L.S., 1997. Structural features off southwestern Taiwan. Marine Geology 137 (3-4), 305-319.

Liu, T.K., Hsieh, S., Chen, Y.G., and Chen, W.S., 2001. Thermo-kinematic evolution of the Taiwan oblique-collision mountain belt as revealed by zircon fission track dating. Earth and Planetary Science Letters 186, 45-56.

Lu, C.Y, 1992. The development of the vein system in central Taiwan: a case study of the section from Kukuan to Tekee along the Central Cross Island highway. J. Geol. Soc. China, 35 (1), 77-94.

Mayer, L., 1986. Tectonic geomorphology of escarpments and mountain fronts. In: Active Tectonics, National Academy Press, Washington DC, pp. 125-135.

Pautot, G., Rangin, C., Briais, A., Tapponnier, P., Beuzart, P., Lericolais, G., Mathieu, X., Wu, J., Han, S., Li, H., Lu, Y., Zhao, J., 1986. Spreading direction in the central South China Sea. Nature 321; 6066, 150-154.

Rau, R.J and Wu, F.T., 1995. Tomographic imaging of lithospheric structures under Taiwan. Earth and Planetary Science Letters 133, 517-532.

Rau, R.J., and Wu, F.T., 1998. Active tectonics of Taiwan Orogeny from focal mechanisms of small-to-moderate-sized earthquakes. TAO 9 (4), 755-778.

Ritter D.F., Kochel, R.C., and Miller, J.R., 2002. Process Geomorphology. 4th ed. McGraw-Hill, New York, 560 p.

Rowley, D.B. and Kidd W.S.F., 1981. Stratigraphic relationships and detrital composition of the medial Ordovician flysch of western New-England – implications for the tectonic evolution of the Taconic orogeny. J. of Geology 89 (2), 199-218.

Seno, T., Moriyama, T., Stein, S., Woods, D.F., Demets, C., Argus, D.F., Gordon, R., 1987. Redetermination of the Philippine Sea Plate motion. Eos, Transactions, American Geophysical Union 68 (44), 1474.

Sibuet, J.C. and Hsu, S.K., 1997. Geodynamics of the Taiwan arc-arc collision. Tectonophysics 274, 221-251.

Strahler, A.N., 1952. Dynamic basis of geomorphology. GSA Bull. 63, 923-938.

Suppe, J., 1984. Kinematics of arc-continent collision, flipping of subduction, and back-arc spreading near Taiwan. Memoir of the Geological Society of China 6, 21-33.

Sung, Q., Lu, M.T., Tsai, H., and Liew, P.M., 1997. Discussion on the genetics and the correlation of river terraces in Taiwan. J. of the Geol. Soc. of China 40 (1), 31-45.

Teng, L.S., 1990. Geotectonic evolution of late Cenozoic arc-continent collision in Taiwan. Tectonophysics 183, 57-76.

Teng, L.S., Lee, C.T., Tsai, Y.B., and Hsiao, L.-Y., 2000. Slab breakoff as a mechanism for flipping of subduction polarity in Taiwan. Geology 28 (2), 155-158.

Tillman, K.S., Byrne, T., and Lu, C.Y., 1992. Pre-collision extensional structures from the central range, Taiwan: Implications for the kinematic evolution of the south China margin. Acta Geologica Taiwanica 30, 11-26.

Tillman, K.S. and Byrne, T.B., 1995. Kinematic analysis of the Taiwan Slate Belt. Tectonics 14 (2), 322-341.

Tillman, K.S. and Byrne, T.B., 1996. Out-of sequence thrusting in the Taiwan slate belt. J. Geol. Soc. China 39 (2), 189-208.

Wells, S.G., Bullard, T.F., Menges, C.C., Drake, P.G., Karas, P.A., Kelson, K.I., Ritter, J.B., and Wesling, J.R., 1988. Regional variation in tectonic geomorphology along a segmented convergent plate boundary, Pacific coast of Costa Rica. Geomorphology 1, 239-265.

Willemin, J.H. and Knuepfer, L.K., 1994. Kinematics of arc-continent collision in the eastern Central Range of Taiwan inferred from geomorphic analysis. JGR 99, B10, 20267-20280.

Willett, S.D, Fisher, D., Fuller, C., Yeh, E.C., and Lu, C.Y, 2003. Erosion rates and orogenic-wedge kinematics in Taiwan inferred from fission-track thermochronometry. Geology 31 (11), 945-948.

Wiltschko, D.V., Hung, J.H., Fang, P., and Bock, Y., 2002. Motion along the Eurasian-Philippine Sea Plate boundary in the Longitudinal Valley, Taiwan from GPS, Eos Trans. AGU, 83 (47), Fall Meet. Suppl., Abstract T61B-1257, 2002.

Yeh, Y.H., Barrier, E., Lin, C.H., and Angelier, J., 1991. Stress Tensor analysis in the Taiwan area from focal mechanisms of earthquakes. Tectonophysics 200, 267-280.

Yen, T.P. and Tien, P.L., 1986. Chaochou fault in southern Taiwan. Proceedings of the Geological Society of China 29, 9-22.

Yu, S.B., Chen, H.Y., and Kuo, L.C., 1997. Velocity field of GPS stations in the Taiwan area. Tectonophysics 274, 41-59.

APPENDIX A

FIELD FABRIC MEASUREMENTS

Table 1. Northern field measurements

A. Planar measurements (Figure 7, a. and c)

Strike	Dip	Type	Strike	Dip	Type	Strike	Dip	Type
140	67W	BDG	40	78NW	BDG	11	83 NW	BDG
40	32E	BDG	35	72S	BDG	65	61 SE	BDG
50	28S	BDG	135	61W	BDG	112	43 SW	BDG
245	32SE	BDG	220	51E	BDG	358	84 SW	BDG
200	54E	BDG	171	38W	BDG	20	68 SE	BDG
213	53W	BDG	10	90	BDG	48	56 SE	BDG
45	27SE	BDG	150	64S	BDG	44	56 SE	BDG
162	72W	BDG	65	51S	BDG	174	36S	FOL
205	41E	BDG	189	90	BDG	45	56SE	FOL
115	30N	BDG	209	88E	BDG	10	65S	FOL
40	90	BDG	43	67E	BDG	220	39S	FOL
20	55E	BDG	210	68	BDG	35	25S	FOL
166	41N	BDG	340	49W	BDG	240	30SE	FOL
61	52NW	BDG	236	84W	BDG	73	23E	FOL
224	23SE	BDG	264	43 SE	BDG	65	35S	FOL
60	30S	BDG	81	35 SE	BDG	55	30S	FOL
227	26E	BDG	236	90	BDG	32	43E	FOL
35	35E	BDG	54	88 NW	BDG	32	60SE	FOL
46	33SE	BDG	204	73 NW	BDG	11	68W	FOL
25	61E	BDG	90	80 N	BDG	180	43E	FOL
38	64SE	BDG	110	45 NE	BDG	209	85E	FOL
245	31S	BDG	222	55 SE	BDG	25	41E	FOL
43	66SE	BDG	46	70 NW	BDG	20	58SE	FOL
25	59S	BDG	195	36 SE	BDG	30	61E	FOL
230	63E	BDG	25	36 SE	BDG	15	51SE	FOL
70	44SE	BDG	15	34 SE	BDG	50	68E	FOL
65	60SE	BDG	66	39 SE	BDG	230	41SE	FOL
61	79E	BDG	60	58 SE	BDG	207	61SE	FOL
50	52SE	FOL	320	29 NE	FOL	160	53N	SS
53	71W	FOL	60	65 SE	FOL	109	48S	SS
219	85W	FOL	85	56 SE	FOL	219	79N	SS
220	85W	FOL	250	56 SE	FOL	231	79S	SS
201	88E	FOL	320	32 NE	FOL	9	81 NW	SS
188	53W	FOL	169	51N	SS	6	85 SE	SS
260	79S	FOL	135	39E	SS	350	70 NE	SS

Table 1A. continued.

Strike	Dip	Type	Strike	Dip	Type	Strike	Dip	Type
345	48W	FOL	61	44S	SS	22	77 NW	SS
50	63E	FOL	27	45SE	SS	9	44 SE	SS
185	45W	FOL	205	60E	SS	30	43 SE	SS
190	46W	FOL	15	54E	SS	20	35 SE	SS
200	21W	FOL	174	39NE	SS	220	39 SE	SS
330	42S	FOL	42	57NW	SS	230	42 SE	SS
260	45SE	FOL	20	79E	SS	90	77 S	SS
315	28 SW	FOL	195	86E	SS	190	26 SE	SS
41	39 NW	FOL	238	79W	SS	73	26 NW	SS
110	42 NE	FOL	212	60NW	SS	145	71 SE	SS
70	43 NW	FOL	58	64S	SS	225	32 SE	SS
111	88 SW	FOL	215	82E	SS	150	76 SW	SS
155	70 NE	FOL	80	85N	SS	50	76 SE	SS
9	57 SE	FOL	65	86E	SS	51	51 NW	SS
15	48 SE	FOL	326	85N	SS	180	28 E	SS
4	61 SE	FOL	233	53E	SS			
338	80 NE	FOL	228	66E	SS			
211	58 SE	FOL	78	87N	SS			
215	58 SE	FOL	131	75S	SS			
200	61 SE	FOL	72	90	SS			
210	15 SE	FOL	252	61S	SS			
340	27 SW	FOL	315	41NE	SS			
21	38 SE	FOL	175	79W	SS			

B. Linear measurements (Figure 7, b. and d)

Trend	Plunge	Type	Trend	Plunge	Type	Trend	Plunge	Type
175	58S	FA	190	70S	FA	179	20S	SLK
195	5S	FA	215	25S	FA	40	43N	SLK
10	30N	FA	215	25S	FA	135	0	SLK
190	25S	FA	310	34W	FA	11	22 NE	SLK
60	20NE	FA	295	30W	FA	105	41 SE	SLK
210	10S	FA	295	20NW	FA	150	38 SE	SLK
220	8SW	FA	170	28S	FA	10	35 NE	SLK
72	10NE	FA	215	19 SW	FA	105	34 SE	SLK
225	32SE	FA	148	39 SE	FA	193	15 SW	SLK
110	28SE	FA	195	42 SW	FA	318	29 NW	SLK
98	21SE	FA	200	42 SW	FA	105	46 SE	SLK
100	16SE	FA	230	42 SW	FA	200	76 SW	SLK
135	33SE	FA	81	35E	SLK	223	03 SW	SLK
190	31S	FA	72	41E	SLK	95	43 SE	SLK
35	0	FA	120	44E	SLK	125	35 SE	SLK
195	22S	FA	93	54E	SLK	100	40 SE	SLK
190	50S	FA	130	31SE	SLK	130	61 SE	SLK
30	?	FA	120	31SE	SLK	260	04 SW	SLK
209	62S	FA	130	77E	SLK	300	36 NW	SLK
245	12SW	FA	320	75N	SLK	140	74 SE	SLK
190	43S	FA	10	50N	SLK	332	51 NW	SLK
190	40S	FA	318	52NW	SLK	140	19 SE	SLK
180	13S	FA	135	59SE	SLK			
180	80S	FA	60	15NE	SLK			
150	61	FA	340	41N	SLK			
5	32N	FA	228	0	SLK			
200	36S	FA	251	20SW	SLK			
180	18S	FA	78	9NE	SLK			
180	70S	FA	50	39NE	SLK			

Table 2. Middle field measurements

A. Planar measurements (Figure 7, e. and g.)

Strike	Dip	Type	Strike	Dip	Type	Strike	Dip	Type	Strike	Dip	Type
60	20S	BDG	55	19E	FOL	280	29 SW	FOL	182	56 NW	FOL
180	90	BDG	180	9W	FOL	50	35 NW	FOL	198	27 NW	FOL
120	82N	BDG	104	37S	FOL	163	27 SW	FOL	220	43SE	SS
89	80N	BDG	160	35W	FOL	302	19 SW	FOL	40	40SE	SS
184	52E	BDG	275	17S	FOL	135	32 SW	FOL	20	53 SE	SS
155	62E	BDG	95	21S	FOL	235	38 SE	FOL	284	60 SW	SS
169	47E	BDG	280	28S	FOL	71	71 NW	FOL	30	54 SE	SS
190	26E	BDG	270	15S	FOL	20	39 NW	FOL	53	38 NE	SS
222	83SE	BDG	65	10E	FOL	300	08 NE	FOL	38	42 SE	SS
340	65 SW	BDG	135	20W	FOL	30	27 NW	FOL	356	80 NW	SS
130	41 SW	BDG	145	29W	FOL	295	30 SW	FOL	10	80 NW	SS
251	55 NW	BDG	105	32S	FOL	290	31 SW	FOL	325	31 SW	SS
30	51 SE	BDG	80	19S	FOL	260	26 SE	FOL	321	29 SW	SS
40	75 SE	BDG	262	38SW	FOL	72	30 SE	FOL	288	70 SW	SS
158	37 SW	BDG	74	34S	FOL	79	35 SE	FOL	188	24 NW	SS
154	37 SE	BDG	89	26S	FOL	80	14 SE	FOL	183	30 NW	SS
122	84 NE	BDG	69	33S	FOL	251	30 SE	FOL			
188	84 SE	BDG	247	24S	FOL	81	35 SE	FOL			
323	29S	FOL	120	21S	FOL	170	15 SW	FOL			
90	26S	FOL	85	62S	FOL	280	34 SW	FOL			
100	38SW	FOL	286	52 SW	FOL	96	35 SW	FOL			
129	31SW	FOL	108	33 SW	FOL	95	21 SW	FOL			
175	49W	FOL	285	49 SE	FOL	48	79 SE	FOL			
79	35SE	FOL	272	42 SW	FOL	230	73 SE	FOL			
168	27SW	FOL	70	23 SE	FOL	16	49 SE	FOL			
213	39S	FOL	110	35 SE	FOL	155	47 SW	FOL			
40	11S	FOL	320	30 SW	FOL	175	74 SW	FOL			
30	44SE	FOL	120	20 SW	FOL	174	58 SW	FOL			

B. Linear measurements (Figure 7, f. and h.)

Trend	Plunge	Type	Trend	Plunge	Type
200	20S	SLK	180	28S	FA
195	19S	SLK	115	34E	FA
215	5S	SLK	290	2W	FA
130	42SE	SLK	240	22S	FA
191	45 SW	SLK	180	10S	FA
56	34 NE	SLK	190	16S	FA
260	29 SW	SLK	210	12SW	FA
25	04 NE	SLK	175	25SE	FA
35	74 NE	SLK	170	35S	FA
205	12SW	FA	170	31S	FA
240	15S	FA	155	63SE	FA
160	36S	FA	180	36S	FA
205	32S	FA	184	21S	FA
100	4E	FA	174	24S	FA
190	21S	FA	205	15S	FA
270	11W	FA	240	28SW	FA
110	12E	FA			

Table 3. Southern field measurements

A. Planar measurements (Figure 7, i. and k.)

Strike	Dip	Type	Strike	Dip	Type	Strike	Dip	Type	Strike	Dip	Type
240	24S	BDG	211	61 SE	BDG	222	44E	FOL	51	71E	FOL
190	10E	BDG	241	42 SE	BDG	59	44SE	FOL	10	71E	FOL
9	55E	BDG	18	28 SE	BDG	227	51S	FOL	20	36SE	FOL
192	25E	BDG	141	48 NE	BDG	205	49E	FOL	160	41E	FOL
229	48E	BDG	175	35 NE	BDG	218	22E	FOL	15	48E	FOL
47	75S	BDG	22	33 SE	BDG	45	48S	FOL	10	29	FOL
60	71SE	BDG	249	43SE	FOL	210	35S	FOL	5	64W	FOL
180	33E	BDG	21	30SE	FOL	220	37SE	FOL	355	31E	FOL
338	30E	BDG	212	41SE	FOL	228	35S	FOL	210	62E	FOL
10	69W	BDG	270	68S	FOL	230	46S	FOL	171	32E	FOL
355	47E	BDG	255	55S	FOL	215	41S	FOL	31	19E	FOL
57	37 SE	BDG	30	53E	FOL	235	59SE	FOL	32	63 SE	FOL
201	35 SE	BDG	250	32E	FOL	246	34S	FOL	246	56 SE	FOL
201	26 SE	BDG	265	51S	FOL	30	65E	FOL	240	74 SE	FOL
210	35 SE	BDG	248	43SE	FOL	231	52S	FOL	249	57 SE	FOL
320	26 NE	BDG	250	33SE	FOL	230	24E	FOL	74	45 SE	FOL
218	10 NW	BDG	245	43SE	FOL	40	60E	FOL	30	40 SE	FOL
210	07 NW	BDG	264	45SE	FOL	42	29E	FOL	216	37 SE	FOL
198	20 SE	BDG	220	43SE	FOL	10	33E	FOL	201	36 SE	FOL
270	15 S	BDG	240	42E	FOL	199	30E	FOL	240	47 SE	FOL
154	10 SW	BDG	54	45SE	FOL	199	55E	FOL	108	06 SW	FOL
108	26 NE	BDG	250	36S	FOL	85	49S	FOL	100	13 SW	FOL
355	07 NE	BDG	190	38E	FOL	210	35S	FOL	236	15 SE	FOL
45	25 NW	BDG	50	40E	FOL	220	65E	FOL	335	46 NE	FOL
21	60 SE	BDG	58	39S	FOL	55	59W	FOL	192	22 NW	SS
192	39 SE	BDG	230	41SE	FOL	225	53S	FOL	315	42 SW	SS
220	09 SE	BDG	55	23SE	FOL	159	55E	FOL	170	75 SW	SS
196	15 SE	BDG	53	56SE	FOL	105	19S	FOL	59	48 NW	SS
30	36 SE	FOL	95	26 SW	FOL	32	40 SE	SS	211	33 SE	SS
205	27 SE	FOL	45	39 SE	FOL	244	25 SE	SS	273	11 NE	SS
76	11 SE	FOL	238	51 SE	FOL	46	25 SE	SS	120	26 SW	SS
164	21 NE	FOL	42	30 SE	FOL	224	33 SE	SS	174	23 NE	FOL
92	15 SW	FOL	170	38E	SS	78	49 SE	SS	230	22 SE	FOL
20	17 SE	FOL	220	40?	SS	315	39 SW	SS	177	25 NE	FOL
40	53 SE	FOL	245	77N	SS	120	38 NE	SS	31	35 SE	FOL

Table 3A. continued.

Strike	Dip	Type	Strike	Dip	Type	Strike	Dip	Type
38	47 SE	FOL	38	57SE	SS	184	61 SE	SS
250	30 SE	FOL	329	45N	SS	101	76 NE	SS
250	41 SE	FOL	28	46E	SS	76	59 SE	SS
40	40 SE	FOL	190	63E	SS	175	58 NE	SS
40	57 SE	FOL	195	55E	SS	161	64 NE	SS
225	65 SE	FOL	37	48E	SS	162	56 NE	SS
38	45 SE	FOL	42	38S	SS	173	46 NE	SS
48	46 SE	FOL	10	58E	SS	17	50 SE	SS
54	54 SE	FOL	55	55S	SS	170	11 NE	SS
320	27 NE	FOL	215	70E	SS	2	38 SE	SS
354	37 NE	FOL	225	70E	SS	42	26 SE	SS
180	57 E	FOL	205	73E	SS	105	86 SW	SS
58	47 SE	FOL	125	67S	SS	345	11 SW	SS
52	46 SE	FOL	76	24N	SS			
52	42 SE	FOL	260	71S	SS			
48	41 SE	FOL	355	43N	SS			
320	13 SW	FOL	162	51E	SS			
242	34 SE	FOL	145	38W	SS			
311	19 SW	FOL	195	35E	SS			
235	30 SE	FOL	258	56S	SS			
225	38 SE	FOL	68	68SE	SS			
45	59 SE	FOL	185	76E	SS			
221	51 SE	FOL	307	59N	SS			
36	31 SE	FOL	35	30 SE	SS			

B. Linear measurements (Figure 7, j. and l.)

Trend	Plunge	Type	Trend	Plunge	Type	Trend	Plunge	Type
83	31E	FA	90	29E	SLK	105	21 SE	SLK
125	27SE	FA	243	33NW	SLK	131	33 SE	SLK
190	9S	FA	62	27E	SLK	158	45 SE	SLK
225	8W	FA	240	18SW	SLK	275	34 NW	SLK
110	20E	FA	290	32N	SLK	335	21 NW	SLK
220	18SW	FA	165	44SE	SLK	24	21 NE	SLK
175	0	FA	200	32S	SLK	48	54 NE	SLK
140	56E	FA	100	32E	SLK	265	41 SW	SLK
120	25E	FA	125	39SE	SLK	336	05 NW	SLK
115	17SE	FA	160	28SE	SLK			
165	25SE	FA	20	16N	SLK			
160	30SE	FA	5	11N	SLK			
230	0	FA	195	22S	SLK			
155	30S	FA	30	36N	SLK			
120	60E	FA	0	29N	SLK			
100	41E	FA	300	20N	SLK			
35	0	FA	170	18S	SLK			
105	0	FA	189	23 SW	SLK			
90	47E	FA	48	11 NE	SLK			
145	31SE	FA	359	18 NW	SLK			
30	0	FA	32	42 NE	SLK			
215	09 SW	FA	45	50 NE	SLK			
224	18 S	FA	108	34 SE	SLK			
285	47 NW	FA	236	10 SW	SLK			
120	39	SLK	355	16 NW	SLK			
150	56S	SLK	70	18 NE	SLK			
355	29N	SLK	65	14 NE	SLK			
115	45SE	SLK	20	09 NE	SLK			
175	45SE	SLK	162	20 SE	SLK			

APPENDIX B

GEOMORPHOLOGY BACKGROUND AND COMPARISON STUDIES

Background

Major surface features in Taiwan include the Longitudinal Valley, the Southern Chaochou Fault, the Pingtung Valley, the Ilan Plane, and the various thrust faults and folds within the Western Foothills Range. A study of Taiwan, by Deffontaines et al., 1994, employed DEM, side-looking airborne radar (SLAR), remote sensing, aerial photographs, and field data to compile a geomorphic map of Taiwan, specifically a map of linear features, presumed to be of tectonic origin. Many of the linear anomalies identified by Deffontaines et al., (1994) are parallel to the orogen and correspond to compressional features, reverse faults, folds and monoclines. Other linear features are oblique and normal to the grain of the mountains and were found to correspond to tension fractures and strike-slip faults. Strike-slip faults were interpreted to be tension fractures reactivated when stress changed from NW-SE directed to E-W directed during the late Pliocene and Late Quaternary (Deffontaines et al., 1994). The lineation study also reveals what are interpreted as four transform fault zones that cut across the Western Foothills and possibly the western Central Range (Deffontaines et al., 1994).

In a study of the Garlock Fault region in Southern California, Bull and McFadden, (1977) defined parameters for mountain front sinuosity (S_{mf}) and valley floor width- height ratio (V_f) and compared values of these parameters along ranges north and south of the fault. They identified three classes of mountain front activity. Active fronts (Class 1) are characterized by S_{mf} values ranging from 1.2-1.6 (very low), low V_f values (around 1.3), low R_e values (0.53), and unentrenched alluvial fans. Moderate or intermediate mountain fronts (Class 2) are characterized by S_{mf} values ranging from 1.8-3.4, moderate V_f values (6.1), larger basins with moderate R_e values (0.69) that indicate more circular basins, and entrenched alluvial fans. Inactive fronts (Class 3) are characterized by high S_{mf} values ranging from 2-7, high V_f values (11.0), and predicted high Re values (not reported in this study). The region north of the Garlock Fault is known to be highly active and includes the Sierra Nevada, Argus, Panamint, and Black Mountains. South of the fault is the inactive Mojave Desert block of relatively old

mountain blocks, buried by basin sediments (Hamilton and Mayers, 1966, in Bull and McFadden, 1977). Class 1 and 2 regions occur north of the Garlock Fault, while class 3 regions are found south, and in the region of the fault (Bull and McFadden, 1977).

Wells et al., 1988, studied geomorphic features, including mountain front sinuosity along the western coast of Costa Rica, north of the Panama Triple Junction. They subdivided their study areas into groups above the subducting Cocos Plate, and those above the subducting Cocos Ridge. The study found that surface features, specifically Smf, stream channel concavity, and dissected facets, indicate increasing tectonic activity and uplift toward the south, as expected in the location of the subducting ridge. Their study shows that geomorphic features in active settings can be used to determine locations of changing plate tectonic settings, such as that from ocean-continent style collision, to ridge-continent collision (Wells et a., 1988).

Another study, by Willemin and Knuepfer, (1994), employed various geomorphic indices to assess activity along the eastern front of the Central Range with the goal of determining the evolution of uplift along the front. They established four geomorphologically distinct sections along the front. The northernmost section, which extends up from the northern tip of the Coastal Range, is characterized by uplift at the range front, while the two middle sections, along the Longitudinal Valley, are characterized by more intense uplift in the interior of the mountain range. Geomorphic indices such as stream length gradient in the southernmost section, which extends down from the southern tip of the Coastal Range, indicate a transient landscape that is not yet adjusted to the tectonic regime (Willemin and Knuepfer, 1994). Range-front activity in the north is attributed to interaction with the colliding Ryukyu subduction system, while the transitional character of the younger, southern section, south of the Coastal Range, may indicate that collision is does not involve the continental basement (Willemin and Knuepfer, 1994).

Chen et al., (2003) also noted along-strike changes in the Taiwan orogen. Using various geomorphic parameters, particularly the SL and Hack indices, for stream profiles along the western boundary of the Western Foothills near Taichung, Chen et al. (2003),

recognized several morphologically distinct segments of the range front that are separated by transform fault zones. They found that the northern segments are more tectonically active than those to the south (Chen at al., 2003). Deffontaines et al., (1994), also noted that deformation is more intense in the north, as indicated by a higher density of structures in the northern third of the island.

Fluvial terraces are another morphologic feature found in abundance throughout the island of Taiwan. These can be very useful in determining the recent uplift history on the local scale. Sung et al. (1997) examined river and fan terraces at various locations around the island and found that, while local tectonics made regional-scale correlation of terrace formations impossible, similarly classified terraces are generally younger in the south, particularly the fan terraces along the mountain front near Chaochou (along the Chaochou Fault) (Sung et al., 1997). A study of river terraces in the Erhjen river basin, in the Western Foothills east and slightly north of the field area for this study, found that the region has undergone active tilting/doming during the Holocene. The recognition and characterization of other actively forming structures in the Western Foothills, such as the Pakuashan Anticline (Delcaillau et al., 1998), has been enhanced with geomorphic study. Similar study may be applied to the Central Range, which through geodetic survey is also known to be actively uplifting.

Comparison Studies

A study of the Garlock Fault in southern California, by Bull and McFadden (1977) is the basis for similar geomorphic studies of fault-bounded mountain fronts. Silva et al. (2003) apply the same parameters defined by Bull and McFadden (1977), S_{mf} and V_f to study mountain fronts in varying tectonic regimes in southeastern Spain. Their data indicate that these combined parameters are useful in assessing mountain front activity in a variety of settings and that different tectonic settings produce characteristic ranges of S_{mf} and V_f.

Wells et al., 1988, studied geomorophic features, including mountain front sinuosity along the western coast of Costa Rica, north of the Panama Triple Junction. They subdivided their study areas into groups above the subducting Cocos Plate, and those above the subducting Cocos Ridge. The study found that surface features, specifically S_{mf}, stream channel concavity, and dissected facets, indicate increasing tectonic activity and uplift toward the south, as expected in the location of the subducting ridge. Their study shows that geomorphic features in active settings can be used to determine locations of changing plate tectonic settings, such as that from ocean-continent style collision, to ridge-continent collision (Wells et a., 1988).

APPENDIX C

GEOMORPHOLOGY DATA TABLES

Table 4. Geomorphic Data for major drainages of the southwest Slate Belt region (Figure 9 and 10)

Label	Distance from south	Area	Basin Spacing	Long Axis	Circular Diameter	Elongation Ratio	Norther half of basin	Basin Asymmetry
	(km)	(km^2)	(km)	(m)	(m)	Diameter/ long axis		100*(N sub/Area(m))
5	138.45	38.01		10107	6958.52	0.69	22.32	41.29
4	132.41	63.27	6.03	11511	8977.96	0.78	30.75	51.40
11	130.25	3.43	2.17	3640	2089.15	0.57	1.92	43.97
6	129.18	12.50	1.07	6533	3990.07	0.61	7.01	43.88
10	126.87	9.70	2.31	4509	3515.47	0.78	3.31	65.91
0	119.91	130.66	6.96	19354	12901.33	0.67	53.80	58.83
8	115.40	5.65	4.51	3986	2681.64	0.67	2.80	50.45
7	113.53	7.04	1.86	4335	2995.31	0.69	2.17	69.18
9	110.05	7.05	3.48	4970	2996.19	0.60	2.39	66.03
1	108.73	31.40	1.32	13537	6324.60	0.47	10.77	65.70
2	103.92	20.14	4.81	8893	5064.55	0.57	6.56	67.40
3	95.28	374.08	8.64	29983	21829.74	0.73	172.82	53.80
13	89.01	13.32	6.27	5377	4118.71	0.77	4.27	67.94
14	83.08	93.40	5.93	16345	10907.84	0.67	55.44	40.64
15	76.95	424.63	6.13	30091	23257.80	0.77	206.75	51.31
16	67.14	44.77	9.81	7584	7552.23	1.00	24.90	44.38
17	55.47	139.83	11.67	17771	13346.57	0.75	63.21	54.79
18	45.81	123.55	9.66	11985	12545.71	1.05	64.89	47.48
19	36.98	87.44	8.83	13815	10553.86	0.76	50.17	42.62
20	32.03	30.70	4.96	8766	6253.94	0.71	13.72	55.31
21	26.83	125.39	5.20	15553	12638.77	0.81	52.13	58.42
23	23.10	10.97	3.73	5335	3737.55	0.70	5.07	53.80
22	20.11	99.09	2.99	17794	11235.46	0.63	99.09	60.84
See Figure	-	9 A, B	10 A		-	10 B		10 C

Table 5. 5th order sub basin size (Figure 9B)

Label	Distance from south (km)	Area (km^2)
0	103.00	147.27
1	101.96	108.74
2	74.60	298.01
4	74.45	97.43
3	66.27	43.20
6	55.11	125.81
5	45.17	120.87
9	36.34	89.15
8	26.92	126.00
7	19.48	94.71

Table 6. 4th order sub basin size (Figure 9B)

Label	Distance (km)	Area (km^2)
0	138.522	37.64241092
2	132.633	63.67799792
6	119.884	131.8723402
1	113.154	13.29133757
7	112.345	19.46713085
4	110.727	13.45719301
3	110.727	15.8009289
5	108.527	31.11301174
8	100.955	41.740604
12	100.955	60.53168524
11	99.661	45.90242767
9	88.044	13.37610805
15	85.521	39.28952113
14	85.521	30.60118836
10	81.897	92.93550232
13	80.764	39.75065988
16	73.289	41.83000647
19	73.289	32.42762371
17	66.171	18.22076757
18	66.171	21.2913829
21	56.269	72.56362504
20	56.259	43.87853224
22	46.724	48.26041116
24	45.724	41.13857659
29	40.771	23.24185188
23	40.771	10.18806338
26	36.887	18.22870777
28	33.263	18.44356366
27	33.263	14.02799158
25	31.451	21.72870381
32	28.054	28.43273181
33	21.938	13.32814019
30	21.938	14.94307327
31	21.615	10.39199662
34	20.417	7.027673046

Table 7. 3rd order sub basin size (Figure 9B)

Label	Distance from south (km)	Area (km^2)	Label	Distance from south (km)	Area (km^2)	Label	Distance from south (km)	Area (km^2)
0	135.33	9.17	39	111.51	12.29	7	89.23	6.67
1	135.33	8.71	44	110.34	10.83	8	89.23	7.87
138	131.52	3.04	26	110.21	7.12	52	88.86	3.91
137	130.26	7.93	37	110.04	6.35	53	88.86	5.47
136	129.22	12.65	133	110.04	3.44	59	88.36	3.08
2	129.09	6.99	132	107.94	3.81	58	88.29	4.75
3	129.09	2.83	134	107.94	5.92	25	88.09	5.45
131	129.09	9.12	30	104.51	4.45	10	85.39	6.31
24	126.42	5.16	45	103.47	12.84	9	84.53	8.52
135	122.12	18.57	47	103.34	4.29	11	84.53	4.30
5	120.65	6.90	48	103.34	4.08	63	82.09	2.36
6	120.45	8.28	46	103.20	3.85	60	81.89	10.80
35	120.45	13.89	40	103.14	9.33	12	81.36	15.18
4	120.35	7.48	72	101.90	2.67	15	81.16	15.22
32	120.35	4.35	31	99.17	8.73	61	81.06	14.96
34	120.35	6.07	74	98.40	2.85	13	79.69	6.75
29	115.85	5.42	75	98.40	7.68	14	79.69	7.99
33	114.81	7.31	51	96.73	11.82	18	77.25	11.86
36	114.48	4.99	49	95.27	5.93	19	77.25	5.85
38	114.48	5.96	50	95.27	8.21	23	74.35	6.45
41	114.01	3.37	57	94.53	11.75	22	73.88	4.52
27	113.58	6.98	73	94.53	2.91	21	73.35	7.08
42	112.88	10.69	56	90.56	25.67	17	72.62	8.83
43	111.54	11.13	56	90.56	25.67	20	72.62	12.99
28	111.51	5.44	62	90.56	8.41	16	69.11	12.72
68	69.11	4.37	91	36.19	2.30	117	22.18	1.32
64	68.71	1.85	93	35.99	1.61	118	21.72	1.30
65	68.71	10.98	92	35.96	1.04	124	21.42	9.83
66	66.28	2.61	106	35.33	2.22	127	21.22	3.68
67	66.28	18.95	97	33.69	4.30	130	20.78	3.25
69	62.98	9.71	105	33.19	4.76	123	20.71	3.23
70	62.88	6.40	108	33.19	3.06	129	20.61	3.66
71	60.11	15.04	95	33.16	0.67	128	17.21	1.97

Table 7. Continued

Label	Distance from south (km)	Area (km^2)	Label	Distance from south (km)	Area (km^2)
80	55.94	10.39	96	33.16	1.39
79	55.44	3.66	109	32.69	6.67
81	55.44	7.00	99	32.52	4.07
84	53.70	12.68	110	32.32	4.29
78	52.07	7.20	100	32.06	3.47
82	52.07	4.39	98	29.62	5.06
86	50.03	6.70	111	28.49	3.30
85	47.47	8.08	112	28.49	2.14
83	46.73	8.17	113	28.14	4.66
76	45.53	9.32	120	27.92	4.31
77	45.53	7.71	107	27.05	12.15
103	41.90	17.95	114	26.55	7.21
89	41.87	3.03	122	24.68	1.79
88	41.26	4.34	126	24.68	1.47
87	40.86	3.14	115	23.45	2.73
94	39.86	6.75	125	23.45	3.20
101	38.36	1.83	119	22.78	7.16
102	38.36	1.82	121	22.78	3.13
90	36.19	1.91	116	22.18	2.78
139	17.21	1.84			

Table 8. Stream gradient data

A. Distance from mouth to specific elevations along the stream channel

Elevation of stream channel	200	400	600	800	1000	1200	1400	1600	1800	2000	2200	2400	2600	2800
Label														
0	3.00	5.20	6.20	6.60	8.20	9.50	11.00	12.20	13.30	13.80	14.40	14.80	15.10	15.20
1	4.50	8.00	9.70	10.70	12.00	13.60	14.30	15.10	15.60	15.90	16.40			
2	1.60	3.30	4.50	5.40	6.10	6.80	7.40	7.70	7.90	8.10				
3	1.20	1.90	2.50	2.90	3.30	3.90	4.10							
4	7.00	15.90	19.90	22.00	25.10	27.40	27.80	28.10	28.50	28.90	29.20	29.50	29.70	
5	1.30	2.50	3.30	4.10	4.40									
6	1.50	2.70	3.40	3.90	4.30									
7	1.70	2.90	3.50	3.90										
8	4.10	8.60	10.10	11.00	11.40									
9	3.10	4.50	6.00	6.90	7.30	7.60								
10	5.00	30.00	35.60	39.00	40.70	42.90	44.20	45.30	46.80	48.70	49.10	49.70		
11	2.00	2.70	3.30	3.70										
12	4.60	16.10	24.50	26.80	27.70	28.30	28.70	28.90	29.20	29.40				
13	9.00	25.80	34.10	42.60	45.00	46.90	49.90	51.00	51.80	52.20	52.50			
14	7.80	15.00	17.10	18.40	18.90	19.10	19.50	19.80	20.00	20.20				
15	4.20	6.60	7.90	8.50	9.00	9.30	9.70							
16	4.80	6.80	7.60	8.30	8.70	9.10	9.30	9.60						
17	7.00	16.10	19.40	21.10	21.80	22.20	22.70	23.10	23.40					
18	7.10	11.50	12.90	13.30	14.20	14.60	15.10	15.30	15.50					
19	9.80	15.00	17.60	18.50	19.10	19.60	19.80							
20	9.80	15.50	16.90	17.80	18.30	18.70	19.10							
21	6.00	7.60	9.60	10.40	10.70	11.00								
22	6.00	7.40	9.00	9.70	9.90									
Elevation of stream channel	200	400	600	800	1000	1200	1400	1600	1800	2000	2200	2400	2600	2800
23	14.20	19.80	22.10	23.20										
24	14.20	18.70	19.70											
25	4.50	5.70												
26	15.00	21.30												

B. Stream gradient at specific elevations along the stream channel (Figure 11)

Elevation of stream channel	200	400	600	800	1000	1200	1400	1600	1800	2000	2200	2400	2600	2800
Label														
0	0.07	0.08	0.10	0.12	0.12	0.13	0.13	0.13	0.14	0.14	0.15	0.16	0.17	0.18
1	0.04	0.05	0.06	0.07	0.08	0.09	0.10	0.11	0.12	0.13	0.13			
2	0.13	0.12	0.13	0.15	0.16	0.18	0.19	0.21	0.23	0.25				
3	0.17	0.21	0.24	0.28	0.30	0.31	0.34							
4	0.03	0.03	0.03	0.04	0.04	0.04	0.05	0.06	0.06	0.07	0.08	0.08	0.09	
5	0.15	0.16	0.18	0.20	0.23									
6	0.13	0.15	0.18	0.21	0.23									
7	0.12	0.14	0.17	0.21										
8	0.05	0.05	0.06	0.07	0.09									
9	0.06	0.09	0.10	0.12	0.14	0.16								
10	0.04	0.01	0.02	0.02	0.02	0.03	0.03	0.04	0.04	0.04	0.04	0.05		
11	0.10	0.15	0.18	0.22										
12	0.04	0.02	0.02	0.03	0.04	0.04	0.05	0.06	0.06	0.07				
13	0.02	0.02	0.02	0.02	0.02	0.03	0.03	0.03	0.03	0.04	0.04			
14	0.03	0.03	0.04	0.04	0.05	0.06	0.07	0.08	0.09	0.10				
15	0.05	0.06	0.08	0.09	0.11	0.13	0.14							
16	0.04	0.06	0.08	0.10	0.11	0.13	0.15	0.17						
17	0.03	0.02	0.03	0.04	0.05	0.05	0.06	0.07	0.08					
Elevation of stream channel	200	400	600	800	1000	1200	1400	1600	1800	2000	2200	2400	2600	2800
18	0.03	0.03	0.05	0.06	0.07	0.08	0.09	0.10	0.12					
19	0.02	0.03	0.03	0.04	0.05	0.06	0.07							
20	0.02	0.03	0.04	0.04	0.05	0.06	0.07							
21	0.03	0.05	0.06	0.08	0.09	0.11								
22	0.03	0.05	0.07	0.08	0.10									
23	0.01	0.02	0.03	0.03										
24	0.01	0.02	0.03											
25	0.04	0.07												
26	0.01	0.02												

Tabel 9. Valley Floor Width-Height Ratio data

Major basin label	Distance from south (km)	Vfw (km)	Eld (km)	Erd (km)	Esc (km)	Vf
5	138.45	0.15	1.80	2.27	1.00	0.04
4	132.41	0.13	1.60	2.38	0.92	0.03
6	129.18	0.05	1.48	1.98	1.13	0.02
10	126.87	0.10	0.45	0.45	0.20	0.10
0	119.91	0.65	1.83	1.85	0.53	0.12
8	115.40	0.05	0.38	0.43	0.10	0.04
7	113.53	0.25	1.37	1.18	0.92	0.17
9	110.05	0.10	0.90	0.95	0.55	0.07
1	108.73	0.15	1.13	0.82	0.52	0.08
2	103.92	0.18	1.37	0.88	0.38	0.06
3	95.28	0.50	1.20	0.82	0.18	0.15
13	89.01	0.10	0.95	0.48	0.22	0.05
14	83.08	0.15	1.02	0.82	0.13	0.05
15	76.95	0.80	1.20	1.02	0.13	0.21
16	67.14	0.10	0.95	0.53	0.17	0.04
17	55.47	0.35	1.00	0.62	0.13	0.13
18	45.81	0.60	0.52	0.63	0.10	0.32
19	36.98	0.90	0.27	0.37	0.03	0.79
20	32.03	0.30	0.40	0.50	0.07	0.20
21	26.83	0.30	0.47	0.47	0.03	0.17
23	23.10	0.10	0.32	0.47	0.07	0.08
22	20.11	1.00	0.68	0.28	0.05	0.58
See Figure						12 A

Table 10. Mountain Front Sinuosity data

Segment Length	Distance from south (km)	Total Length (m)	DMG (m)	Smf
20 km	146.54	6368.55	5857.99	0.08
	140.68	22934.39	20105.69	0.12
	120.58	25213.71	20236.30	0.20
	100.34	21918.08	20185.33	0.08
	80.16	26698.25	20165.73	0.24
	59.99	40556.12	20345.85	0.50
	39.64	35648.80	20068.02	0.44
	19.58	14112.43	10242.60	0.27
	9.33	14159.38	9333.68	0.34
10 km	145.73	14579.35	12078.62	0.17
	133.65	11885.89	10165.32	0.14
	123.48	14834.66	11351.43	0.23
	112.13	11966.64	10254.30	0.14
	101.88	10934.11	10636.55	0.03
	91.24	11581.23	10168.71	0.12
	81.07	12239.77	10321.77	0.16
	70.75	14716.31	10171.35	0.31
	60.58	20187.85	10340.83	0.49
	50.24	20394.55	10220.50	0.50
	40.02	23884.55	10205.01	0.57
	29.81	12079.76	10184.54	0.16
	19.63	14165.68	10294.89	0.27
	9.33	14159.38	9333.68	0.34
See Figure				12 B

VITA

Name: Lauren E. Hassler

Address: 354 Devonwood Dr.

Boone, NC 28607

Parents: Reginald and Diane Hassler

Education: MS Geology, August 2004, Texas A&M Univeristy, College Station TX

BS Geology, May 2001, Appalachian State University, Boone NC

Professional Experience:

Teaching Assistant Department of Geology and Geophysics
Texas A&M University, 2001-2003
Teaching Assistant, Summer Field Camp, Northern Italy
Department of Geology
Appalachian State University, 2001
Research Assistant, Department of Geology,
Appalachian State University, 1998-2000
Part-Time Patroller, Sugar Mountain Ski Resort
Sugar Mountain, North Carolina, 1998-2001

Publications:

Hassler, L.E. and Cowan, E.A., 2001. Characteristics of Ice-Rafted Pebbles from the Continental Rise Sediment Drifts West of the Antarctic Peninsula (ODP Sites 1095, 1096, and 1101). ODP Scientific Results, Leg 178. (www.odp.tamu.edu/publications/178_SR/chap_11/chap_11.htm)

Abstracts:

Hassler, L.E. and Wiltschko, D.V., A Multi-Source Assessment of Motion Along the Chaochou Fault, Southern Taiwan. In Eos. Trans. AGU, Fall Meet. Suppl., 2003 © American Geophysical Union. (in press).

Hassler, L.E. and Wiltschko, D.V. Characterizing the Chaochou Fault: Results of a Preliminary Field Study of Southern Taiwan. In Eos. Trans. AGU, 83 (47) Fall Meet. Suppl., Abstract T61B-1275, 2002 © American Geophysical Union.

Hassler, L.E., Cowan, E.A, and Wolf-Welling, Thomas, 2000. Changing Antarctic Peninsula Glaciation Over the Last 3Ma: Clues from Ice-Rafted Sand and Pebbles Deposited on the Continental Rise Sediment Drifts, GSA Abstract no.50420. (rock.geosociety.org/docs/absindex/annual/2000/50420.htm)